



AIAA 2004-2186
Avian Wings

Tianshu Liu, K. Kuykendoll, R. Rhew, S. Jones

NASA Langley Research Center
Hampton, VA 23681-2199

**24th AIAA Aerodynamic Measurement
Technology and Ground Testing
Conference**
28 June – 1 July 2004/Portland, Oregon

Avian Wings

Tianshu Liu[†], K. Kuykendoll^{*}, R. Rhew[‡] and S. Jones^{**}
 NASA Langley Research Center
 Hampton, VA 23681

Abstract

This paper describes the avian wing geometry (Seagull, Merganser, Teal and Owl) extracted from non-contact surface measurements using a three-dimensional laser scanner. The geometric quantities, including the camber line and thickness distribution of airfoil, wing planform, chord distribution, and twist distribution, are given in convenient analytical expressions. Thus, the avian wing surfaces can be generated and the wing kinematics can be simulated. The aerodynamic characteristics of avian airfoils in steady inviscid flows are briefly discussed. The avian wing kinematics is recovered from videos of three level-flying birds (Crane, Seagull and Goose) based on a two-jointed arm model. A flapping seagull wing in the 3D physical space is re-constructed from the extracted wing geometry and kinematics.

1. Introduction

Inspired by bird flight, early aviation researchers have studied avian wings as the basics of developing man-made flight vehicles. This methodology is clearly seen in the work of Lilienthal [1] and Magnan [2]. This may be partially the reason why early aircraft designers like the Wright brothers tended to use thin airfoils by simply simulating bird wings. However, this situation was dramatically changed since thick airfoils (such as Göttingen and NACA airfoils) designed based on theoretical and experimental methods of aerodynamics achieved much higher lift-to-drag ratio at Reynolds numbers in airplane flight. Thus, study of avian wings becomes a marginalized topic that only interests a few avian biologists and zoologists. Nachtigall and Wieser [3] measured the airfoil sections of a pigeon's wing. Oehme and Kitzler [4] measured the planform of 14 avian wings and gave an empirical formula for avian wing planforms.

Recently, there is renewed interest in low-Reynolds-number flight and flapping flight in the aerospace community due to the need of developing micro-air-vehicles (MAVs). Hence, it is worthwhile to revisit the problem of the geometry and aerodynamics of avian wings. In this paper, we measure the surface geometry of several avian wings using a 3D laser scanning system. Based on these

measurements, we extract the basic geometrical properties of a wing such as the camber line, thickness distribution, planform and twist distribution, and generate 3D wing surfaces. The aerodynamic performance of the avian wing airfoils in steady inviscid flow is calculated in comparison with typical low-Reynolds-number airfoils. We explain how to recover the avian wing kinematics from videos of a level-flying bird. The present paper provides useful data for further biomimetic study of low-Reynolds-number wings and flapping wings for MAVs.

2. 3D Laser Scanner on FARO Arm

Figure 1 shows a FARO Arm (FARO Technologies, Inc.) to which a NVision's 3D non-contact laser scanner is attached for wing surface measurements. The FARO Arm is a high accuracy hand-held mechanical device with an exchangeable probe, that is used to measure objects and features to create data of a surface. When the NVision 3D Scanner is attached and aligned to the arm, the capability of acquiring high-density point cloud data of a surface becomes available. On the FARO arm, the position of the scanner relative to a given coordinate system is known accurately. The accuracy of the surface data is within 0.041mm and data can be given in the coordinate system chosen. It is the fastest, smallest, and lightest hand-held non-contact scanning system available.

Operating with ModelMaker software, the system works on the principle of laser stripe triangulation. A laser diode and stripe generator is used to project a laser line onto the object. The line is viewed at an angle by cameras so that height variations in the object can be seen as changes in the shape of the line. The resulting captured image of the stripe is a profile that contains the shape of the object. The software processes video data to capture surface shape in real time at over 23,000 points per second. The NVision Scanner uses digital camera synchronization to ensure precise measurements. It can scan a large variety of materials and colors including black, and work in almost any lighting conditions. ModelMaker is Windows-compatible software that outputs data in a variety of CAD formats. This system can generate millions of data points. For illustration, Figure 2 shows data cloud of the surface of a seagull wing obtained using this system. In this study, we only use a subset of data, that is, wing-cross-section data at selected spanwise locations.

[†] Research Scientist, ASOMB, AAAC, MS 238, Member AIAA, t.liu@larc.nasa.gov, 757-864-4639.

^{*} Quality Assurance Specialist, Research Hardware Validation and Verification Branch.

[‡] Engineer, AMSSB, AAAC, MS 238, Member AIAA.

^{**} Biologist, AMSSB, AAAC, MS 238

3. Data Processing

The upper and lower surface of an airfoil are expressed as addition and subtraction of the camber line and thickness distribution, $z_{upper} = z_{(c)} + z_{(t)}$ and $z_{lower} = z_{(c)} - z_{(t)}$, respectively. To extract the mean camber line from measurements, we use the Birnbaum-Glauert camber line [5]

$$\frac{z_{(c)}}{c} = \frac{z_{(c)max}}{c} \eta (1-\eta) \sum_{n=1}^3 S_n (2\eta-1)^{n-1}, \quad (1)$$

where $\eta = x/c$ is the normalized chordwise coordinate and $z_{(c)max}$ is the maximum camber coordinate, and c is the local wing chord. The thickness distribution is given by [5]

$$\frac{z_{(t)}}{c} = \frac{z_{(t)max}}{c} \sum_{n=1}^4 A_n (\eta^{n+1} - \sqrt{\eta}), \quad (2)$$

where $z_{(t)max}$ is the maximum thickness coordinate (the maximum thickness is $2z_{(c)max}$). For a given set of measured data of wing contour, a rotation and translation transformation is first applied in order that the geometrical angle-of-attack becomes zero and the leading edge of the wing section is located at the origin of the local coordinate system. Therefore, the local wing chord, twist angle, $z_{(c)max}$, $z_{(t)max}$, relative position of the leading and trailing edges can be determined. Next, using least-squares estimation, we can obtain the coefficients S_n and A_n in Eqs. (1) and (2). These quantities are functions of the normalized spanwise coordinate $\xi = 2y/b$. Table 1 shows the averaged coefficients for the camber line and thickness distribution for the Seagull, Merganser, Teal and Owl wings. Details of how to extract these coefficients from measurements are discussed in the following sections.

The chord can be expressed as

$$\frac{c}{b/2} = \frac{c_0}{b/2} [F_{OK}(\xi) + F_{corr}(\xi)], \quad (3)$$

where c_0 is the root chord of a wing. The function $F_{OK}(\xi)$ is a correlation given by Oehme and Kitzler [4] for avian wings, which is defined as $F_{OK}(\xi) = 1$ for $\xi \in [0, 0.5]$ and $F_{OK}(\xi) = 4\xi(1-\xi)$ for $\xi \in [0.5, 1]$. The correction function for the deviation of an individual wing from

$F_{OK}(\xi)$ is $F_{corr}(\xi) = \sum_{n=1}^5 E_n (\xi^{n+2} - \xi^8)$, where the

coefficients E_n are to be determined. Table 2 shows the coefficients for the planform of the Seagull, Merganser, Teal and Owl wings. The maximum camber line and thickness coordinates $z_{(c)max}$ and $z_{(t)max}$ can be described by appropriate empirical functions of $\xi = 2y/b$. Similarly, the relative position and kinematics of the 1/4-chord line of a wing to the fixed body coordinate system can be described by a dynamical system $(x_{c/4}, y_{c/4}, z_{c/4})/(b/2) = \mathbf{f}_{c/4}(t)$,

where t is time. As an approximate model, an avian wing can be described as a multiple jointed rigid arm system and its kinematics can be determined [6, 7]. In this paper, for simplicity, we adopt a two-jointed rigid arm system to describe the 1/4-chord line of an avian wing rather than exactly simulating the more complicated skeleton structure of an avian wing. The local twist angle of the airfoil section around the 1/4-chord line can be given by $\theta = f_{\theta}(2x_{c/4}/b, 2y_{c/4}/b, 2z_{c/4}/b)$. When the geometric and kinematic parameters in the above relations are given, a flapping wing can be computationally generated and the wing kinematics can be simulated.

4. Avian Wing Geometry

4.1. Seagull

Figure 3 shows a photograph of the Seagull wing used for this study. The coefficients S_n and A_n in Eqs. (1) and (2) for the camber line and thickness distribution are extracted from measurements of the Seagull wing. It is found that they do not show the systematic behavior as a function of the spanwise location, as shown in Fig. 4. Particularly, a considerable variation in A_n exists. The averaged values of S_n along the span in Eq. (1) are $S_1 = 3.8735$, $S_2 = -0.807$ and $S_3 = 0.771$. The averaged coefficients A_n in Eq. (2) for the thickness distribution are $A_1 = -15.246$, $A_2 = 26.482$, $A_3 = -18.975$ and $A_4 = 4.6232$. Figure 5 shows the normalized camber line and thickness distribution for the Seagull wing generated by using the above averaged coefficients. These distributions exhibit the averaged airfoil of the Seagull wing over $\xi = 2y/b = 0.166 - 0.772$. For $2y/b > 0.772$, the primaries are separated such that no single, continuous airfoil exists. The least-squares estimation residuals in fitting local airfoils $z_{(c)}/c$ and $z_{(t)}/c$ at different spanwise locations are shown in Fig. 6(a). Similarly, the deviations of the averaged $z_{(c)}/z_{(c)max}$ and $z_{(t)}/z_{(t)max}$ from the local profiles at different spanwise locations are shown in Fig. 6(b).

As shown in Fig. 7, the maximum camber and thickness coordinates $z_{(c)max}$ and $z_{(t)max}$ are functions of the spanwise location $\xi = 2y/b$, which are empirically expressed as $z_{(c)max}/c = 0.14/(1 + 1.333 \xi^{1.4})$ and $z_{(t)max}/c = 0.1/(1 + 3.546 \xi^{1.4})$. Figure 8 shows the planform of the Seagull wing. The distribution of the wing chord, as shown in Fig. 9, can be described by Eq. (3) that is the Oehme and Kitzler's correlation $F_{OK}(\xi)$ plus a correction function $F_{corr}(\xi) = \sum_{n=1}^5 E_n (\xi^{n+2} - \xi^8)$ for local variation, where $E_1 = 26.08$, $E_2 = -209.92$, $E_3 = 637.21$,

$E_4 = -945.68$ and $E_5 = 695.03$. The ratio between the root chord and semi-span is $c_0 / (b/2) = 0.388$. Figure 10 shows the wing twist as a function of the spanwise location, which is expressed as an expansion of the Chebyshev polynomials ($T_1 = \xi$, $T_2 = 4\xi^3 - 3\xi$, and

$$T_3 = 16\xi^5 - 20\xi^3 + 5\xi$$
, i.e., $twist(deg) = \sum_{n=1}^3 D_n T_n(\xi)$,

where $D_1 = 5.2788$, $D_2 = -4.1069$ and $D_3 = -1.8684$. Here the positive sign of the twist denotes that the wing rotates against the incoming flow. Note that the wing twist presented here is not necessarily intrinsic because not only the twist may be changed in preparing the wing specimen, but also the twist is really a time-dependent variable during flapping. Using the above relations obtained from measurements, we generate the surface of the Seagull wing shown in Fig. 11, where a simple two-jointed arm model is used for the 1/4-chord line. Also, we assume that the airfoil section remains the same near the wing tip while the maximum thickness decreases even though the real wing has separated primaries near the wing tip.

4.2. Merganser

Figure 12 shows a photograph of the Merganser wing used for this study. The coefficients S_n and A_n for the camber line and thickness distribution of the Merganser wing are shown in Fig. 13. The averaged values of S_n along the span are $S_1 = 3.9385$, $S_2 = 0.7466$ and $S_3 = 1.840$. The averaged coefficients A_n for the thickness distribution are $A_1 = -23.1743$, $A_2 = 58.3057$, $A_3 = -64.3674$ and $A_4 = 25.7629$. Figure 14 shows the normalized camber line and thickness distribution for the Merganser wing generated by using the above averaged coefficients. The wing thickness is very small (considered to be zero) near the trailing edge ($x/c > 0.9$). The least-squares estimation residuals in fitting local airfoils $z_{(c)}/c$ and $z_{(t)}/c$ at different spanwise locations are shown in Fig. 15(a). The deviations of the averaged $z_{(c)}/z_{(c)max}$ and $z_{(t)}/z_{(t)max}$ from the local profiles at different spanwise locations are shown in Fig. 15(b).

Figure 16 shows the maximum camber and thickness coordinates $z_{(c)max}$ and $z_{(t)max}$ as a function of the spanwise location $\xi = 2y/b$ along with the empirical expressions $z_{(c)max}/c = 0.14 / (1 + 1.333 \xi^{1.4})$ and $z_{(t)max}/c = 0.05 / (1 + 4 \xi^{1.4})$. Figure 17 shows the planform of the Merganser wing. The distribution of the wing chord is shown in Fig. 18 along with the results given by Eq. (3) where the coefficients in $F_{corr}(\xi)$ are $E_1 = 39.1$, $E_2 = -323.8$, $E_3 = 978.7$, $E_4 = -1417.0$ and

$E_5 = 1001.0$. The ratio between the root chord and semi-span is $c_0 / (b/2) = 0.423$. Figure 19 shows the wing twist as a function of the spanwise location, which is expressed as an expansion of the Chebyshev polynomials ($T_1 = \xi$, $T_2 = 4\xi^3 - 3\xi$, and $T_3 = 16\xi^5 - 20\xi^3 + 5\xi$), i.e.,

$$twist(deg) = \sum_{n=1}^3 D_n T_n(\xi)$$
, where $D_1 = 30.9953$,

$D_2 = -3.2438$ and $D_3 = -0.2076$. Figure 20 shows the surface of the Merganser wing generated using the above relations.

4.3. Teal

Figure 21 shows a photograph of the Teal wing used for this study. The averaged values of S_n along the span for the camber line are $S_1 = 3.9917$, $S_2 = -0.3677$ and $S_3 = 0.0239$. The averaged coefficients A_n for the thickness distribution are $A_1 = 1.7804$, $A_2 = -13.6875$, $A_3 = 18.276$ and $A_4 = -8.279$. Figure 22 shows the normalized camber line and thickness distribution for the Teal wing generated by using the above averaged coefficients. The least-squares estimation residual in fitting local airfoils $z_{(c)}/c$ and $z_{(t)}/c$ is less than 0.003. The deviations of the averaged $z_{(c)}/z_{(c)max}$ and $z_{(t)}/z_{(t)max}$ from the local profiles are less than 0.1 and 0.2, respectively.

Figure 23 shows the maximum camber and thickness coordinates $z_{(c)max}$ and $z_{(t)max}$ as a function of the spanwise location $\xi = 2y/b$ along with the empirical expressions $z_{(c)max}/c = 0.11 / (1 + 4 \xi^{1.4})$ and $z_{(t)max}/c = 0.05 / (1 + 4 \xi^{1.4})$. Figure 24 shows the planform of the Teal wing. The distribution of the wing chord is shown in Fig. 25 along with the results given by Eq. (3) where the coefficients in $F_{corr}(\xi)$ are $E_1 = -66.1$, $E_2 = 435.6$, $E_3 = -1203$, $E_4 = 1664.1$ and $E_5 = -1130.2$. The ratio between the root chord and semi-span is $c_0 / (b/2) = 0.545$. The wing twist is less than 2 degrees along the span. Figure 26 shows the surface of the Teal wing generated using the above relations.

4.4. Owl

Figure 27 shows a photograph of the Owl wing. The averaged values of S_n along the span for the camber line are $S_1 = 3.9733$, $S_2 = -0.8497$ and $S_3 = -2.723$. The averaged coefficients A_n for the thickness distribution are $A_1 = -47.683$, $A_2 = 124.5329$, $A_3 = -127.0874$ and $A_4 = 45.876$. Figure 28 shows the normalized camber line and thickness distribution for the Owl wing generated by using the above averaged coefficients. The least-squares

estimation residual in fitting local airfoils $z_{(c)}/c$ and $z_{(t)}/c$ is less than 0.006. The deviations of the averaged $z_{(c)}/z_{(c)max}$ and $z_{(t)}/z_{(t)max}$ from the local profiles are less than 0.1 and 0.2, respectively. Interestingly, the Owl wing is very thin over $x/c = 0.3 - 1.0$ (it is a single layer of the primary feathers) and the thickness distribution is mainly concentrated in the front portion of the airfoil. The wing thickness is considered to be zero near the trailing edge ($x/c > 0.9$).

Figure 29 shows the maximum camber and thickness coordinates $z_{(c)max}$ and $z_{(t)max}$ as a function of the spanwise location $\xi = 2y/b$ along with the empirical expressions $z_{(c)max}/c = 0.04[1 + \tanh(1.8\xi - 0.5)]$ and $z_{(t)max}/c = 0.04/(1 + 1.78\xi^{1.4})$. In contrast to other wings described before, the maximum chamber coordinate for the Owl wing increase along the span. Figure 30 shows the planform of the Owl wing. The distribution of the wing chord is shown in Fig. 31 along with the results given by Eq. (3) where the coefficients in $F_{corr}(\xi)$ are $E_1 = 6.3421$, $E_2 = -7.5178$, $E_3 = -70.9649$, $E_4 = 188.0651$ and $E_5 = -160.1678$. The ratio between the root chord and semi-span is $c_0/(b/2) = 0.677$. The wing twist is less than 2 degrees along the span. Figure 32 shows the surface of the Owl wing generated using the above relations.

5. Aerodynamic Characteristics of Avian Airfoils in Steady Inviscid Flows

Figure 33 shows typical wing sections of the Seagull, Merganser, Teal and Owl at $2y/b = 0.4$. These airfoils are highly cambered. The inviscid pressure coefficient C_p distributions at four angles of attack are shown in Figs. 34, 35, 36 and 37. Figure 38 shows the sectional lift coefficient based on unit chord as a function the angle of attack (AoA) for the Seagull, Merganser, Teal and Owl wings. These results are obtained by using the inviscid/viscous flow analysis code XFOIL for airfoil design [8], which roughly indicate the aerodynamic characteristics of these airfoils. The pressure distributions on the upper surfaces of the Seagull and Merganser wings are relatively flat when AoA is less than 5 degrees. The sectional lift coefficients of at zero AoA for both are larger than one. Figure 39 shows the sectional lift coefficient distributions along the wing span for these wings at AoA = 0 degree. Based on the sectional lift coefficient c_l , we can estimate the normalized circulation distribution $\Gamma(y)/\Gamma_0 = [c(y)/c_0][c_l(y)/c_{l0}]$ shown in Fig. 40, where the subscript '0' denotes the value at the wing root ($2y/b = 0$). The Seagull and Merganser wings have the almost same normalized circulation distributions. The Owl airfoil is particularly interesting, that is basically a thin wing with a thickness distribution concentrated mainly

near the leading edge. Unlike other wings, the c_l distribution for the Owl wing has an increasing behavior as the wing span because the maximum camber coordinate $z_{(c)max}$ increases. As a result, the normalized circulation distribution has a special shape as indicated in Fig. 40. We do not know whether the thin Owl wing and the associated aerodynamic properties are related to quiet flight of an owl [9]. Clearly, the aerodynamic and aeroacoustic implications of the thin Owl wing are worthwhile to be investigated further.

The Seagull and Merganser airfoils are similar to the high-lift low Reynolds number airfoil S1223 described by Selig et al. [10]. Figure 41 shows the S1223 airfoil along with the Seagull and Merganser airfoils with the same the maximum camber line and thickness coordinates ($z_{(c)max}/c = 0.0852$ and $z_{(t)max}/c = 0.0579$). Figures 42 and 43 shows a comparison of the pressure coefficient distributions between the S1223, Seagull and Merganser airfoils. These pressure distributions are similar, but the S1223 airfoil has lower pressure on the upper surface near $x/c = 0.2$ and trailing edge. The sectional lift coefficient as a function of AoA for these airfoils is shown in Fig. 44. When AoA increases beyond a certain value (about 10 degrees), laminar flow separation will take place near the leading edge in a Reynolds number range for birds (4×10^4 to 7×10^5) [11,12]. The separated flow may be reattached due to transition to turbulence that can be facilitated by using artificial boundary layer tripping. Detailed calculation of the separated/reattached flow on these airfoils requires a Navier-Stokes (N-S) solver with accurate transition and turbulence models; computation based on the N-S equation especially for the unsteady flow field around a flapping wing is a topic in further study. Here, we do not intend to conduct such computation without reliable experimental data for comparison. Nevertheless, experimental data for the S1223 airfoil [10] provide a good reference (in a qualitative sense) for the behavior of the Seagull and Merganser airfoils at high angles of attack.

6. Avian Wing Kinematics

6.1. Front-Projected 1/4-Chord Line

For simplicity, we consider the kinematics of a flapping wing as a superposition of the motion of the 1/4-chord line of the wing and relative rotation of local airfoil sections around the 1/4-chord line. From videos of a level-flying bird taken by a camera viewing directly the front of the bird, we are able to approximately recover the front-projected profiles of the 1/4-chord line of the wing at a sequence of times. Figure 45 shows a typical image of a level-flying crane viewed directly from the front and a local coordinate system used for describing the profiles. A front-projected wing in images is a line with a finite thickness that is approximately considered as the front-projected 1/4-chord line. The profile of the front-projected 1/4-chord line of a

flapping wing can be reasonably described by a second-order polynomial

$$\frac{z_{1/4}}{b/2} = A_1(\omega t) \left(\frac{y_{1/4}}{b/2} \right) + A_2(\omega t) \left(\frac{y_{1/4}}{b/2} \right)^2, \quad (4)$$

where the coefficients and the semi-span are given by the Fourier series as a function of the non-dimensional time ωt (ω is the circular frequency of flapping)

$$A_1(\omega t) = C_{10} + \sum_{n=1}^2 [C_{1n} \sin(n\omega t) + B_{1n} \cos(n\omega t)],$$

$$A_2(\omega t) = C_{20} + \sum_{n=1}^2 [C_{2n} \sin(n\omega t) + B_{2n} \cos(n\omega t)],$$

$$\frac{b(\omega t)/2}{\max(b/2)} = C_{b0} + \sum_{n=1}^2 [C_{bn} \sin(n\omega t) + B_{bn} \cos(n\omega t)]. \quad (5)$$

Here, $b/2$ is defined as the semi-span of an orthographically projected flapping wing on the horizontal plane. Therefore, $b/2$ is a time-dependent function in a flapping cycle. The maximum value of $b/2$ is achieved roughly at the moment when a flapping wing is parallel to the horizontal plane. We assume that $\omega t = 0$ corresponds to the position of a wing at the beginning of the down-stroke (or the end of the up-stroke) (see Fig. 45).

6.1.1. Crane

A time sequence of images of a level-flying crane taken by a camera directly from the front of the bird are obtained by digitizing a clip of the video "The Life of Birds" produced by BBC. The profiles of the front-projected wing (or 1/4-chord line) are obtained by manually tracing the wing in digitized images. Eq. (4) is used to fit data of the successive profiles and the coefficients in Eq. (5) are determined. Figure 46 shows the measured profiles of the front-projected 1/4-chord line of a flapping wing of a flying crane and the corresponding polynomial fits at six instants (an interval of $2\pi/5$) in a flapping cycle $\omega t \in [0, 2\pi]$. The profiles can be reasonably described by a second-order polynomial Eq. (4) with the time-dependent coefficients. Figures 47 and 48 show data of the coefficients in Eq. (5) and the orthographically projected semi-span $b/2$ that are fit by the Fourier series, respectively. The coefficients in Eq. (5) extracted from measurements for a flapping wing of a crane are

$$C_{10} = 0.3639, \quad C_{11} = -0.2938, \quad B_{11} = 0.4050,$$

$$C_{12} = -0.0465, \quad B_{12} = -0.0331;$$

$$C_{20} = -0.4294, \quad C_{21} = 0.4469, \quad B_{21} = 0.1442,$$

$$C_{22} = 0.0135, \quad B_{22} = 0.0691;$$

$$C_{b0} = 0.839, \quad C_{b1} = 0.0885, \quad B_{b1} = 0.0301, \quad C_{b2} = -0.0888,$$

$$B_{b2} = -0.0407.$$

Figure 48 shows that the orthographically projected semi-span $b/2$ on the horizontal plane varies with time. At

$\omega t = 0$, the position of the wing is at the beginning of the down-stroke. The wing is approximately parallel to the horizontal plane at $\omega t \approx 2$ and $b/2$ reaches the maximal value. The minimal value of $b/2$ is at $\omega t \approx 3.9$. The down-stroke spans about 62% of a flapping cycle while the up-stroke takes 38% of a cycle. The variation of $b/2$ with time depends on not only the orthographic projection, but also a change of the wing planform due to wing extension and folding during flapping. We calculate the arc length of the front-projected 1/4-chord line as a function of time by using Eqs. (4) and (5). In fact, a change in the arc length of the front-projected 1/4-chord line represents a change of the wing planform due to wing extension and folding. Figure 49 shows the arc length of the projected 1/4-chord line as a function of time for the flapping crane, seagull and goose wings. For a crane, its wing is most extended at $\omega t \approx 2.1$ while it is most folded at $\omega t \approx 4$. The normalized arc length of the front-projected 1/4-chord line is described by the Fourier series

$$\frac{L_{proj}(\omega t)}{\max(L_{proj})} = C_{L0} + \sum_{n=1}^2 [C_{Ln} \sin(n\omega t) + B_{Ln} \cos(n\omega t)]. \quad (6)$$

For the flapping crane wing, the coefficients in Eq. (6) are $C_{L0} = 0.9310$, $C_{L1} = 0.0359$, $B_{L1} = 0.0111$, $C_{L2} = -0.0675$, $B_{L2} = -0.0093$.

This result will be used later to re-construct the wing kinematics based on a two-jointed arm model.

6.1.2. Seagull

Similarly, a time sequence of images of a flying seagull (acquired from Oceanfootage.com) is processed and the profiles of the front-projected 1/4-chord line are recovered. The coefficients in Eq. (5) extracted from measurements for a flapping wing of a seagull are

$$C_{10} = 0.3756, \quad C_{11} = -0.3242, \quad B_{11} = 0.1920,$$

$$C_{12} = 0.0412, \quad B_{12} = -0.1095;$$

$$C_{20} = -0.4674, \quad C_{21} = 0.3631, \quad B_{21} = 0.2884,$$

$$C_{22} = -0.0661, \quad B_{22} = 0.0553;$$

$$C_{b0} = 0.7978, \quad C_{b1} = 0.1751, \quad B_{b1} = 0.0461, \quad C_{b2} = 0.0042,$$

$$B_{b2} = -0.0218.$$

Figure 50 shows the measured profiles of the front-projected 1/4-chord line of a flapping wing of a flying seagull and the corresponding polynomial fits at six instants (an interval of $2\pi/9$) in a flapping cycle. Figures 51 and 52 show data of the coefficients in Eq. (5) and the orthographically projected semi-span $b/2$ that are fit by the Fourier series, respectively.

For the normalized arc length of the front-projected 1/4-chord line of the flapping seagull wing, the coefficients in Eq. (6) are

$$C_{L0} = 0.8718, \quad C_{L1} = 0.1420, \quad B_{L1} = -0.0111,$$

$$C_{L2} = 0.0190, \quad B_{L2} = 0.0113.$$

As shown in Fig. 49, the flapping seagull wing is most extended at $\omega t \approx 1.3$ while it is most folded at $\omega t \approx 5$.

6.1.3. Goose

A time sequence of images of a flying bar-headed goose from the documentary "Winged Migration" is processed and the profiles of the front-projected 1/4-chord line are recovered. The coefficients in Eq. (5) extracted from measurements for a flapping wing of a level-flying goose are

$$\begin{aligned} C_{10} &= 0.4511, & C_{11} &= -0.2819, & B_{11} &= 0.3008, \\ C_{12} &= 0.0254, & B_{12} &= -0.0835; \\ C_{20} &= -0.4605, & C_{21} &= 0.4516, & B_{21} &= 0.1912, \\ C_{22} &= -0.0845, & B_{22} &= 0.1154; \\ C_{b0} &= 0.8999, & C_{b1} &= 0.0666, & B_{b1} &= 0.0126, \\ C_{b2} &= -0.0505, & B_{b2} &= -0.0095. \end{aligned}$$

Figure 53 shows the measured profiles of the front-projected 1/4-chord line of a flapping wing of a flying goose and the corresponding polynomial fits at six instants (an interval of $\pi/5$) in a flapping cycle. Figures 54 and 55 show data of the coefficients in Eq. (5) and the orthographically semi-span $b/2$ that are fit by the Fourier series, respectively.

For the normalized arc length of the front-projected 1/4-chord line of the flapping goose wing, the coefficients in Eq. (6) are

$$\begin{aligned} C_{L0} &= 0.9948, & C_{L1} &= 0.0013, & B_{L1} &= -0.0013, \\ C_{L2} &= -0.0083, & B_{L2} &= 0.0122. \end{aligned}$$

As shown Fig. 49, the normalized arc length of the front-projected 1/4-chord line of the flapping goose wing does not vary much compared with the flapping crane and seagull wings. This means that relatively speaking the goose wing does not extend and fold much during flapping.

6.2. Two-Jointed Arm Model

In general, the skeleton structure is described as a three-jointed arm system. Figure 56 is an X-ray image showing the skeleton structure of a seagull wing. However, for level flapping flight, the wing kinematics can be simplified. In this case, to describe the 1/4-chord line of a flapping wing, we use a two-jointed arm model that consists of two rigid jointed rods. As shown in Fig. 57, Rod 1 rotates around the point O_1 in a body coordinate system where the origin O_1 is located at the wing root and the plane YO_1Z is defined as the rotational plane of Rod 1. Thus, the motion of Rod 1 has only one degree of freedom and the position of Rod 1 is given by the flapping angle ψ_1 . In contrast, the motion of Rod 2 has two degrees of freedom, which is given by the angles ψ_2 and ϕ_2 . In Fig. 57, the line O_2T' is the orthographic projection of the Rod 2 (or the line O_2T) on the plane YO_1Z . The angle ψ_2 is the angle between Rod 1 and the line O_2T' on the plane YO_1Z , which basically

determines the flapping magnitude of Rod 2 relative to Rod 1. The angle ϕ_2 is the angle between Rod 2 and the line O_2T' , which describes the extension and folding of a wing (the outer portion of a wing). Figure 58 shows the projected views of a two-jointed arm system. In Fig. 58(c), the angle $\phi_{2\perp} = \phi_2 / \cos(\psi_1 - \psi_2)$ is the orthographic projection of the angle ϕ_2 on the horizontal plane XO_1Y . The simple two-jointed arm model allows the recovery of 3D kinematics of a flapping wing from measurements of the front-projected 1/4-chord line. In addition, it is a straightforward model for designing a mechanical flapping wing.

The coordinates of the end point O_2 of Rod 1 are

$$X_{O_2} = 0, \quad Y_{O_2} = L_1 \cos(\psi_1), \quad Z_{O_2} = L_1 \sin(\psi_1), \quad (7)$$

where L_1 is the length of Rod 1. The position of Rod 1 is described by

$$\begin{aligned} X &= 0 \\ Z &= Y \tan(\psi_1), \end{aligned} \quad (8)$$

where $Y \in [0, L_1 \cos(\psi_1)]$. The position of Rod 2 is given by

$$\begin{aligned} X &= -(Y - Y_{O_2}) \tan\left(\frac{\phi_2}{\cos(\psi_1 - \psi_2)}\right), \\ Z &= Z_{O_2} + (Y - Y_{O_2}) \tan(\psi_1 - \psi_2) \end{aligned} \quad (9)$$

where $Y \in [L_1 \cos(\psi_1), b/2]$. Note that $b/2$ is the orthographically projected semi-span on the horizontal plane XO_1Y . Therefore, we know that the projected semi-span is $b/2 = L_1 \cos(\psi_1) + L_2 \cos(\phi_2) \cos(\psi_1 - \psi_2)$. In a two-jointed arm system, the normalized arc length of the front-projected 1/4-chord line is

$$\frac{L_{proj}(\omega t)}{\max(L_{proj})} = r_1 + r_2 \cos(\phi_2), \quad (10)$$

where $r_1 = L_1 / \max(L_{proj})$ and $r_2 = L_2 / \max(L_{proj})$ are the relative lengths of Rod 1 and Rod 2.

6.3. Recovery of the Angles ψ_1 , ψ_2 and ϕ_2

A two-jointed arm model uses two pieces of straight line to approximate the profile of the 1/4-chord line of a wing. Since the flapping angles ψ_1 and ψ_2 are on the plane YO_1Z , they can be estimated directly from the measured profile of the front-projected 1/4-chord line, Eq (4), when $r_1 = L_1 / \max(L_{proj})$ and $r_2 = L_2 / \max(L_{proj})$ are given. The angle ϕ_2 can be extracted from the measured arc length of the front-projected 1/4-chord line using Eqs. (10) and (6). Figures 59, 60 and 61 shows the recovered angles ψ_1 , ψ_2 and ϕ_2 as a function of time for the flapping crane, seagull and goose wings, respectively.

The angles ψ_1 , ψ_2 and ϕ_2 are expressed as the Fourier series

$$\begin{aligned}
\psi_1(\omega t) &= C_{\psi 10} + \sum_{n=1}^2 [C_{\psi 1n} \sin(n\omega t) + B_{\psi 1n} \cos(n\omega t)], \\
\psi_2(\omega t) &= C_{\psi 20} + \sum_{n=1}^2 [C_{\psi 2n} \sin(n\omega t) + B_{\psi 2n} \cos(n\omega t)], \\
\phi_2(\omega t) &= C_{\phi 20} + \sum_{n=1}^2 [C_{\phi 2n} \sin(n\omega t) + B_{\phi 2n} \cos(n\omega t)].
\end{aligned}
\tag{11}$$

The estimated coefficients in Eq. (11) for the crane, seagull and goose wings are given below. Here, we assume that $r_1 = 0.5$ and $r_2 = 0.5$. The units of the angles ψ_1 , ψ_2 and ϕ_2 in Eq. (11) are in degrees.

Crane

$$\begin{aligned}
C_{\psi 10} &= 8.3065, & C_{\psi 11} &= -4.4519, & B_{\psi 11} &= 25.3910, \\
C_{\psi 12} &= -1.8092, & B_{\psi 12} &= -0.5889; \\
C_{\psi 20} &= 17.0661, & C_{\psi 21} &= -17.3404, & B_{\psi 21} &= -4.0066, \\
C_{\psi 22} &= -3.7029, & B_{\psi 22} &= -4.5122; \\
C_{\phi 20} &= 32.2311, & C_{\phi 21} &= -8.6004, & B_{\phi 21} &= -0.34280, \\
C_{\phi 22} &= 15.2213, & B_{\phi 22} &= 2.6910.
\end{aligned}$$

Seagull

$$\begin{aligned}
C_{\psi 10} &= 8.4654, & C_{\psi 11} &= -8.5368, & B_{\psi 11} &= 17.8798, \\
C_{\psi 12} &= 1.0898, & B_{\psi 12} &= -4.5880; \\
C_{\psi 20} &= 17.3083, & C_{\psi 21} &= -11.0122, & B_{\psi 21} &= -9.6131, \\
C_{\psi 22} &= 1.3128, & B_{\psi 22} &= -3.0183; \\
C_{\phi 20} &= 38.4179, & C_{\phi 21} &= -28.0553, & B_{\phi 21} &= 0.7664, \\
C_{\phi 22} &= -4.1032, & B_{\phi 22} &= 3.0125.
\end{aligned}$$

Goose

$$\begin{aligned}
C_{\psi 10} &= 12.2528, & C_{\psi 11} &= -3.7150, & B_{\psi 11} &= 21.1873, \\
C_{\psi 12} &= -0.6432, & B_{\psi 12} &= -2.3054; \\
C_{\psi 20} &= 20.0863, & C_{\psi 21} &= -18.6807, & B_{\psi 21} &= -7.3848, \\
C_{\psi 22} &= 1.3467, & B_{\psi 22} &= -6.1507; \\
C_{\phi 20} &= 13.5235, & C_{\phi 21} &= -0.7494, & B_{\phi 21} &= 1.2524, \\
C_{\phi 22} &= 4.3138, & B_{\phi 22} &= -6.3023.
\end{aligned}$$

6.4. Reconstruction of a Flapping Wing

After the wing geometry (the airfoil section, planform, and twist distribution) and the kinematics of the 1/4-chord line of a wing are given, a flapping wing can be re-constructed in the 3D physical space by superimposing the airfoil sections on the moving 1/4-chord line. Note that the wing twist distribution in flapping is not recovered in this paper. Measurements of the dynamical wing twist distribution require considerable videogrammetric processing on a time sequence of images taken from two

cameras simultaneously viewing a flapping wing of a level-flight bird on which a sufficient number of suitably distributed targets are attached. In computational simulations, the wing twist can be treated as a variable to achieve the maximum aerodynamic efficiency. Here, we simply assume that the wing twist is fixed during flapping. Using Eqs. (1), (2), (3), (8), (9) and (11) with the known coefficients for a seagull wing, we re-construct a flapping seagull wing at different instants as shown in Fig. 62.

6. Conclusions

Using a 3D laser scanner, we have measured the surface geometry of the Seagull, Merganser, Teal and Owl wings. From measurements, the airfoil camber line, airfoil thickness distribution, wing planform and twist distribution are extracted. The accuracy of metric measurements using the laser scanner is about 0.041mm. The residual of least-squares fitting for an airfoil section is about $2-10 \times 10^{-3}$ in terms of the normalized coordinate z/c . The estimated coefficients for the camber line and thickness distribution do not exhibit a systematic behavior along the wing span. Thus, the averaged values of these coefficients along the wing span are given, which define the averaged airfoil for an avian wing. The deviation of the local airfoil camber line and thickness distribution from the averaged ones is about 5-20% of their maximum value. The Seagull and Merganser airfoils are similar to high-lift low Reynolds number airfoils. The Teal airfoil has a relatively symmetric thickness distribution around the mid-chord. The Owl airfoil is very thin over $0.3-1.0$ chord and the thickness distribution is mainly concentrated in the front portion of the airfoil. Unlike other wings, the Owl wing has a special circulation distribution along the wing span.

We consider the kinematics of a flapping wing as a superposition of the motion of the 1/4-chord line of the wing and relative rotation of local airfoil sections around the 1/4-chord line. The profiles of the front-projected 1/4-chord line at different instants are measured from videos of a level-flying bird. Then, based on a two-jointed arm model, the kinematics of the 1/4-chord line in the 3D physical space is recovered for the flapping Crane, Seagull and Goose wings. The relevant quantities of the wing kinematics are given in convenient analytical expressions. The wing geometry and kinematics given in this paper are useful for the design of flapping MAVs and experimental and computational studies to understand the fundamental aerodynamic aspects of flapping flight.

References:

- [1] Lilienthal, O., Birdflight as the Basis of Aviation, Markowski International Publishers, Hummestown, PA, 2001.
- [2] Magnan, A., Bird Flight and Airplane Flight, NASA TM-75777, 1980.

- [3] Nachtigall, W. and Wieser, J., Profilmessungen am Taubenflügel, *Zeitschrift für vergleichende Physiologie* 52, pp. 333-346, 1966.
- [4] Oehme, H. and Kitzler, U., On the Geometry of the Avian Wing (Studies on the Biophysics and Physiology of Avian Flight II), NASA-TT-F-16901, 1975.
- [5] Riegels, F. W., *Aerofoil Sections*, Butterworths, London, 1961, Chapters 1 and 7.
- [6] Asada, H. and Slotine, J.-J. E., *Robot Analysis and Control*, John Wiley and Sons, New York, 1986, Chapters 2 and 3.
- [7] Zinkovsky, A. V., Shaluha, V. A. and Ivanov, A. A., *Mathematical Modeling and Computer Simulation of Biomechanical Systems*, World Scientific, Singapore, 1996, Chapters 1 and 2.
- [8] Drela, M., XFOIL: An Analysis of and Design System for Low Reynolds Number Airfoils, Conference on Low Reynolds Number Airfoil Aerodynamics, University of Notre Dame, June 1989.
- [9] Lilley, G. M., A Study of the Silent Flight of the Owl, AIAA Paper 98-2340, Toulouse, France, June 2-4, 1998.
- [10] Selig, M. S., Guglielmo, J. J., Broeren, A. P. and Giguere, P., *Summary of Low-Speed Airfoil Data, Volume 1.*, SoarTech Publications, Virginia Beach, Virginia, 1995, Chapter 4.
- [11] Carmichael, B. H., Low Reynolds Number Airfoil Survey, NASA CR 165803, 1981.
- [12] Lissaman, P. B. S., Low-Reynolds-Number Airfoils, *Ann. Rev. Fluid Mech.*, 15, 1983, pp. 223-239.

Table 1. The Coefficients for Avian Airfoil

	Seagull	Merganser	Teal	Owl
S_1	3.8735	3.9385	3.9917	3.9733
S_2	-0.807	0.7466	-0.3677	-0.8497
S_3	0.771	1.840	0.0239	-2.723
A_1	-15.246	-23.1743	1.7804	-47.683
A_2	26.482	58.3057	-13.6875	124.5329
A_3	-18.975	-64.3674	18.276	-127.0874
A_4	4.6232	25.7629	-8.279	45.876

Table 2. The Coefficients for Wing Planform

	Seagull	Merganser	Teal	Owl
E_1	26.08	39.1	-66.1	6.3421
E_2	-209.92	-323.8	435.6	-7.5178
E_3	637.21	978.7	-1203.0	-70.9649
E_4	-945.68	-1417.0	1664.1	188.0651
E_5	695.03	1001.0	-1130.2	-160.1678

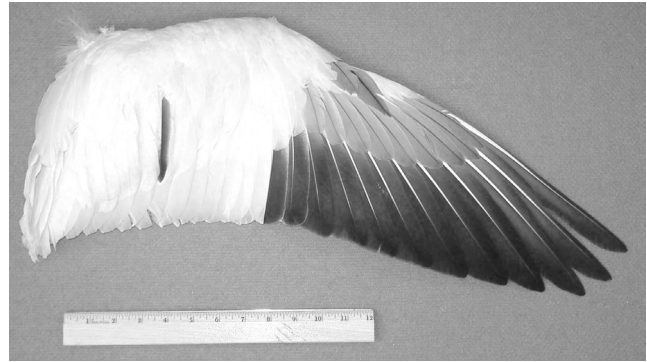


Figure 3. Seagull wing.

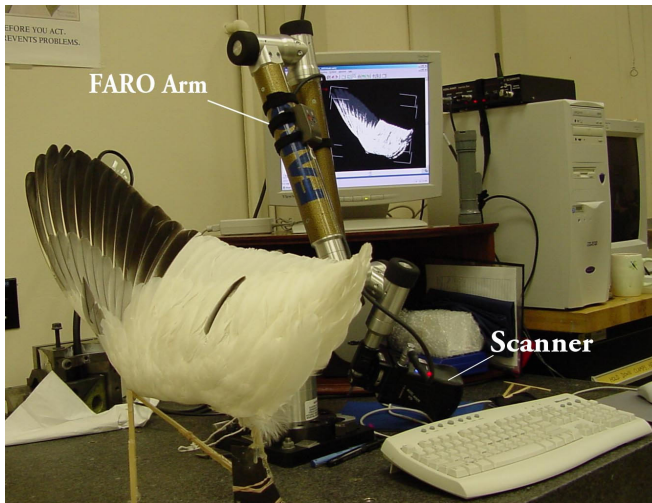


Figure 1. 3D laser scanner and FARO arm for wing surface measurements.



Figure 2. Data cloud of the surface of a seagull wing.

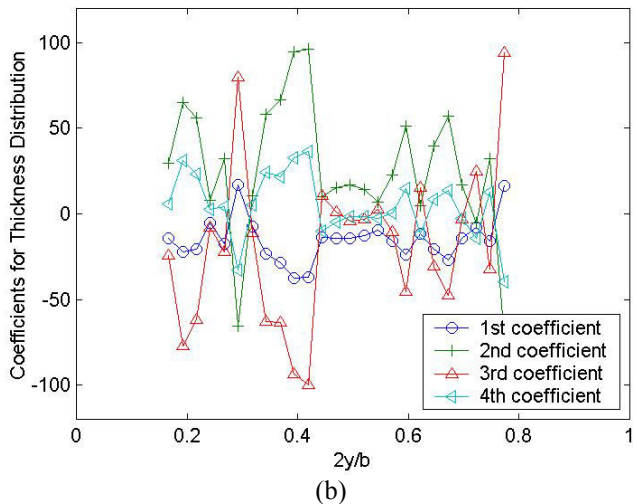
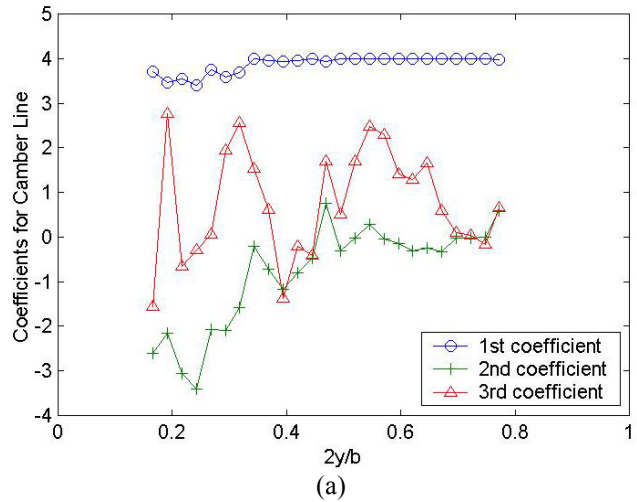


Figure 4. (a) The coefficients for the camber line, (b) The coefficients for the thickness distribution for the Seagull wing.

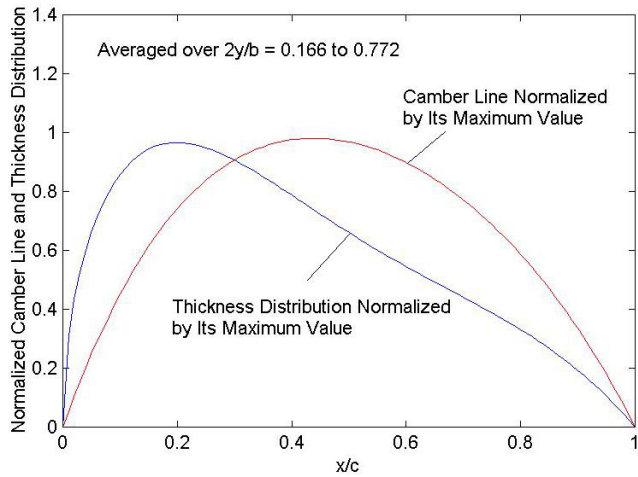


Figure 5. The camber line and thickness distribution of the Seagull wing.

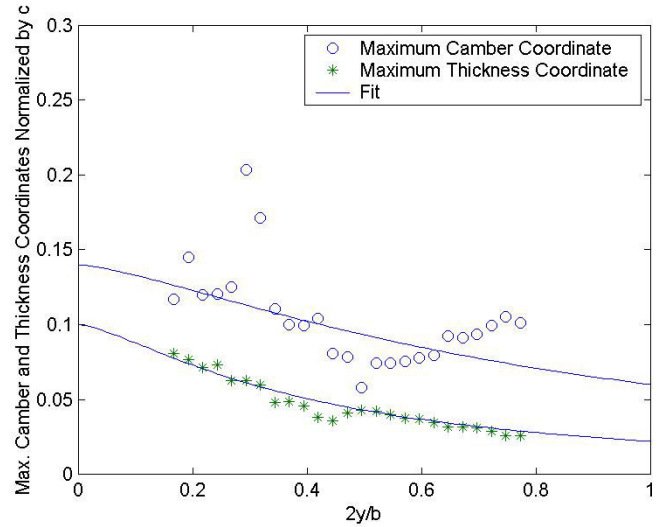
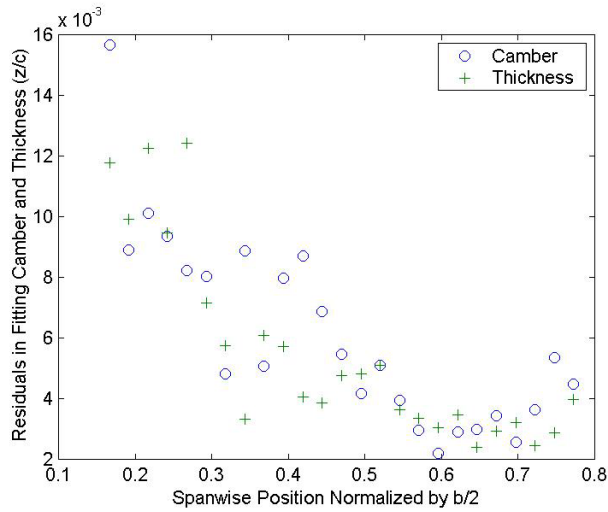
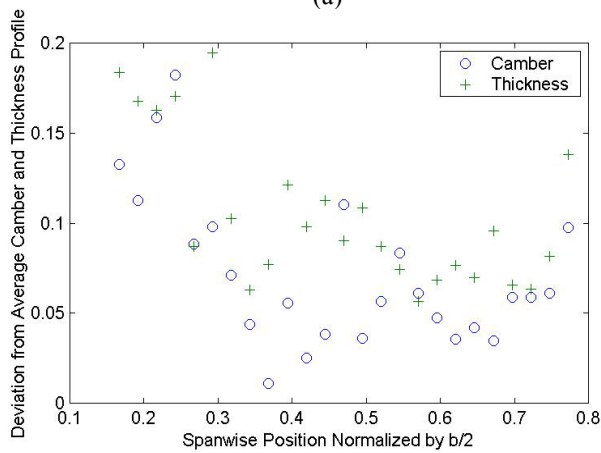


Figure 7. The maximum camber and thickness coordinates as a function of the spanwise location for the Seagull wing.



(a)



(b)

Figure 6. (a) Least-squares residuals of fitting the airfoil sections, (b) Deviation of local profiles from the averaged profile for the Seagull wing.

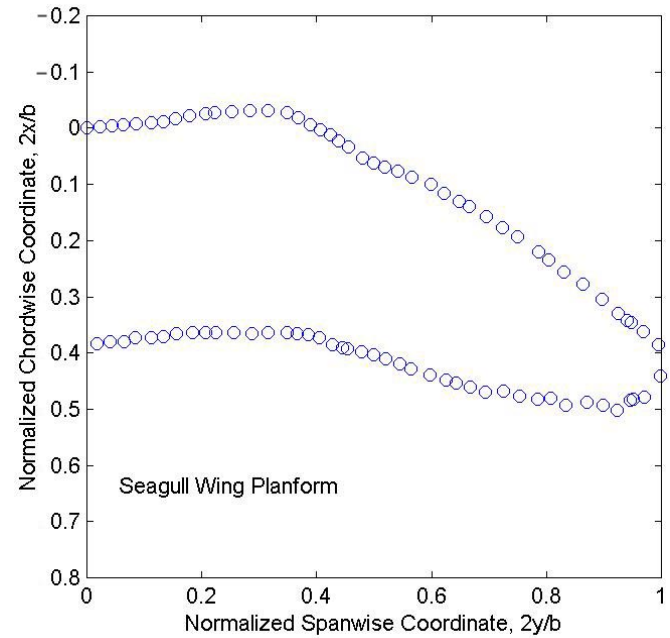


Figure 8. The planform of the Seagull wing.

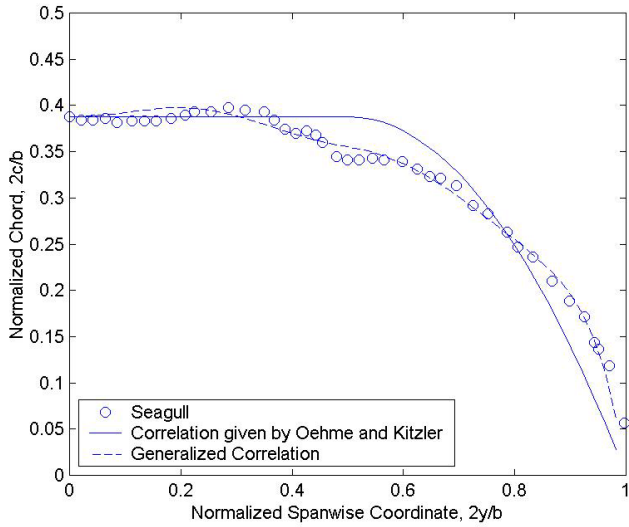


Figure 9. The chord distribution of the Seagull wing.

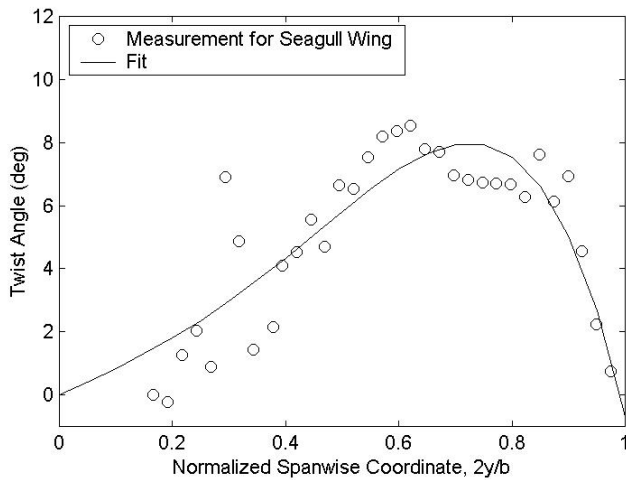


Figure 10. The twist distribution of the Seagull wing.

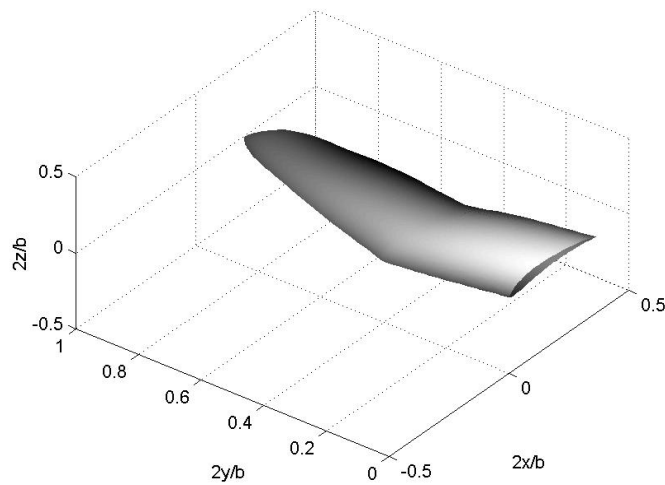


Figure 11. The generated surface of the Seagull wing.



Figure 12. The Merganser wing.

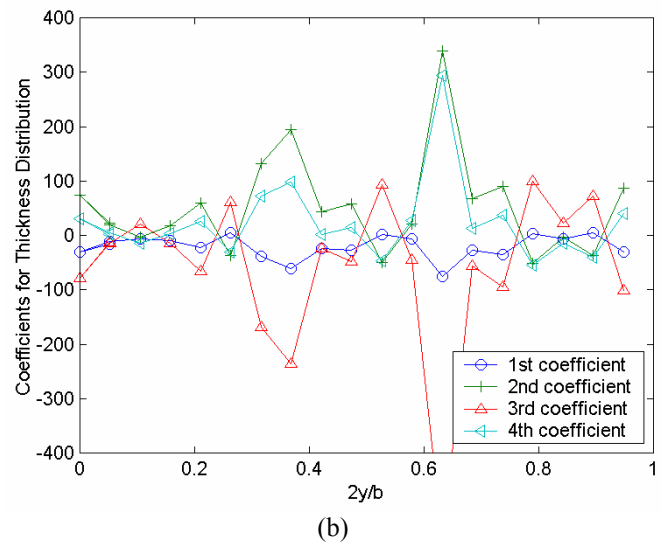
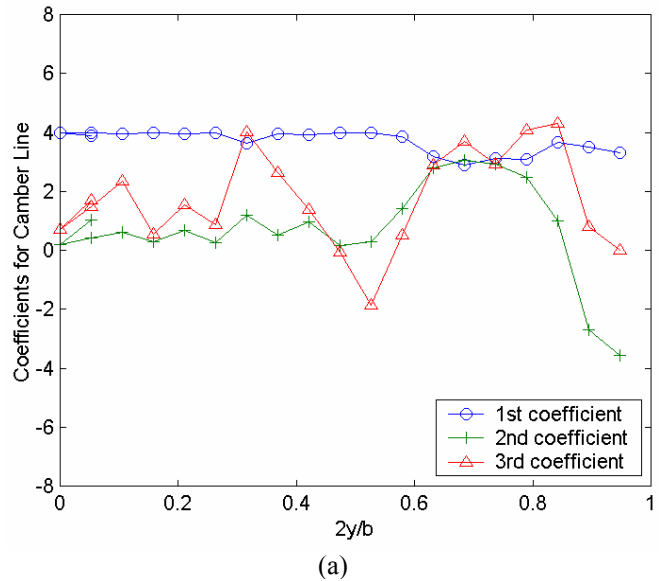


Figure 13. (a) The coefficients for the camber line, (b) The coefficients for the thickness distribution for the Merganser wing.

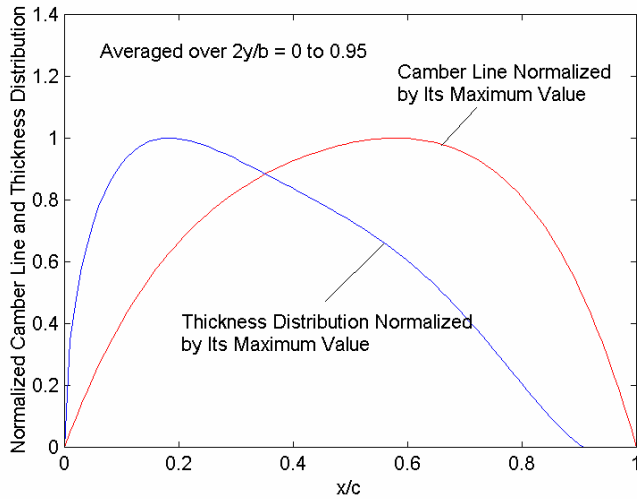
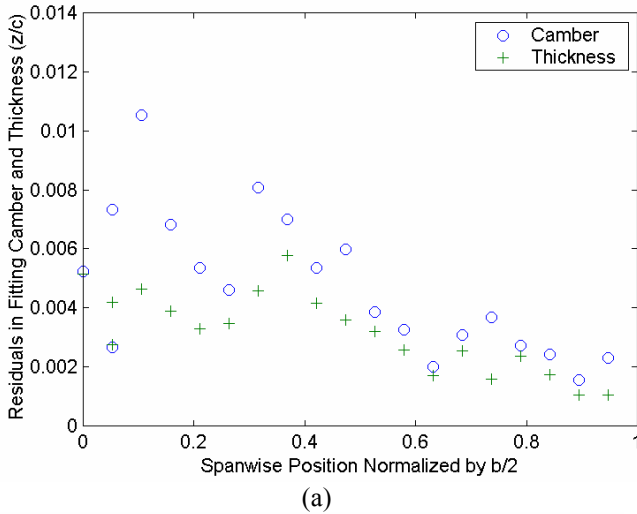
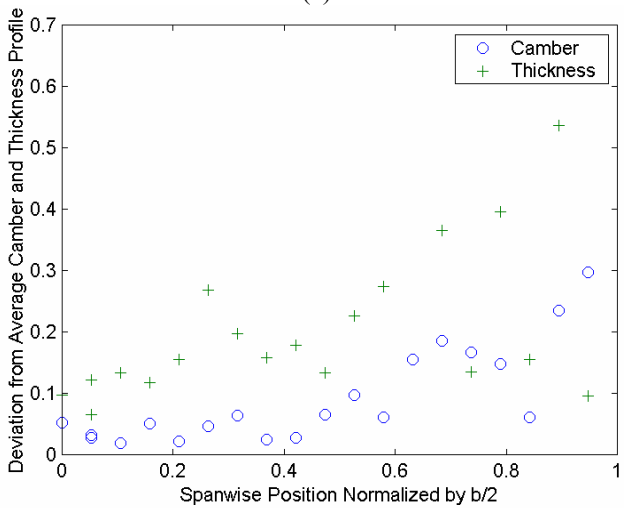


Figure 14. The camber line and thickness distribution of the Merganser wing.



(a)



(b)

Figure 15. (a) Least-squares residuals of fitting the airfoil sections, (b) Deviation of local profiles from the averaged profile for the Merganser wing.

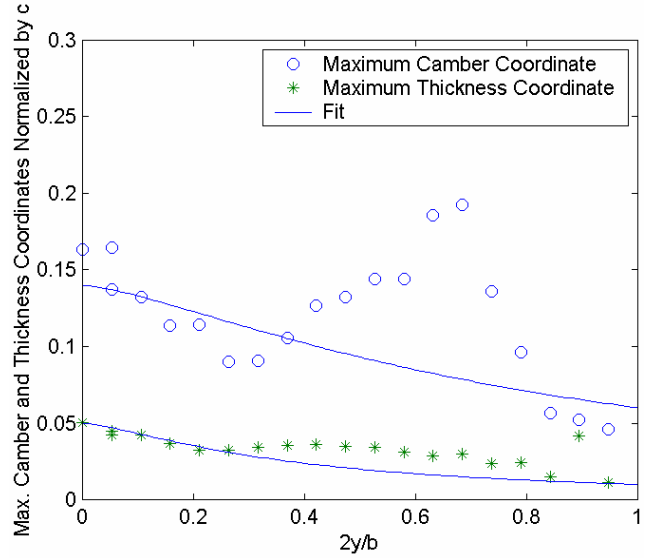


Figure 16. The maximum camber and thickness coordinates as a function of the spanwise location for the Merganser wing.

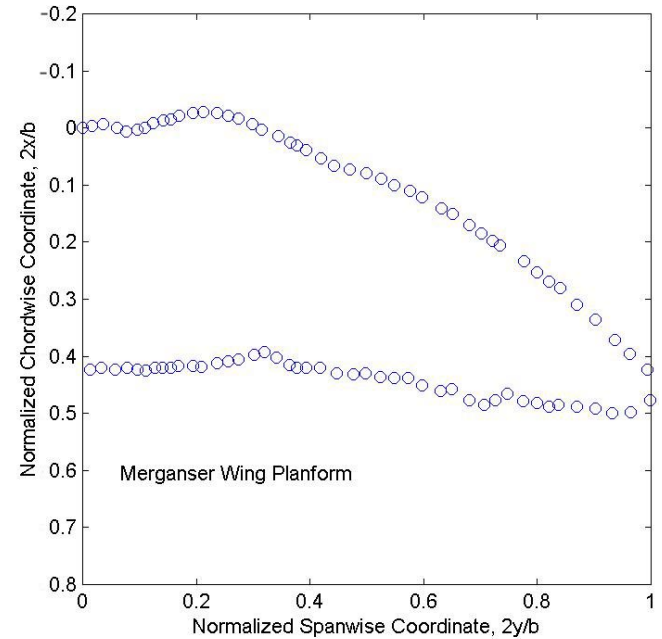


Figure 17. The planform of the Merganser wing.

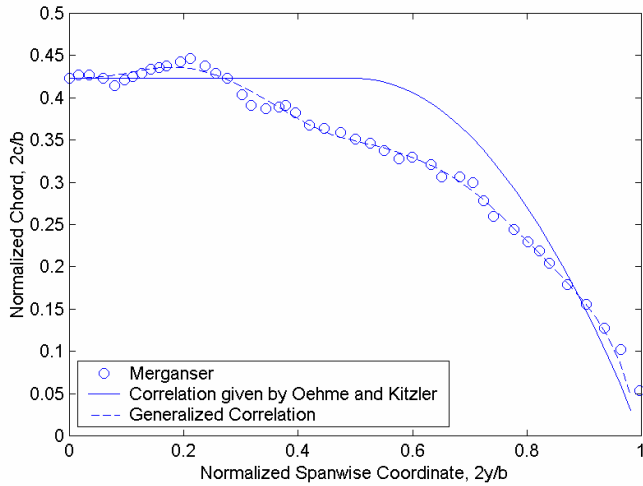


Figure 18. The chord distribution of the Merganser wing.

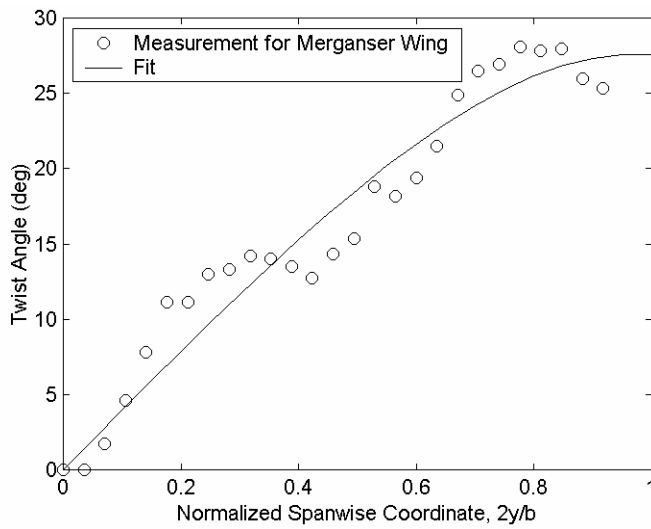


Figure 19. The twist distribution of the Merganser wing.

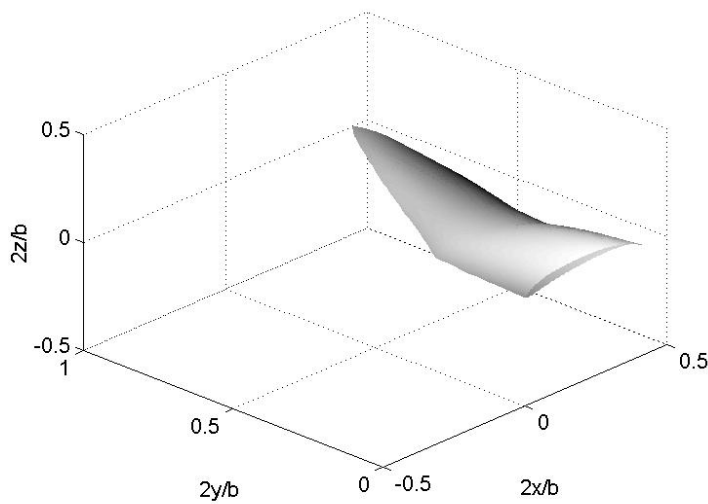


Figure 20. The generated surface of the Merganser wing.



Figure 21. The Teal wing.

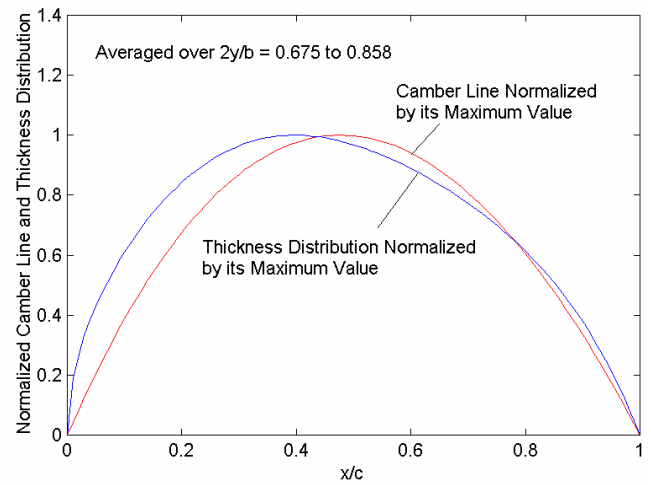


Figure 22. The camber line and thickness distribution of the Teal wing.

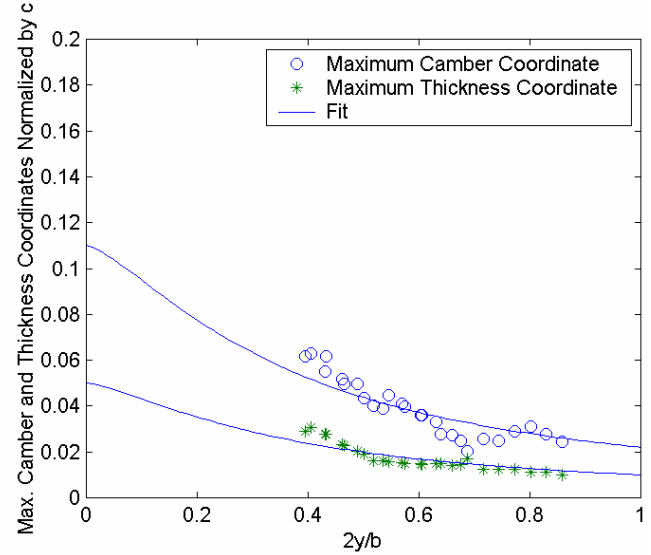


Figure 23. The maximum camber and thickness coordinates as a function of the spanwise location for the Teal wing.

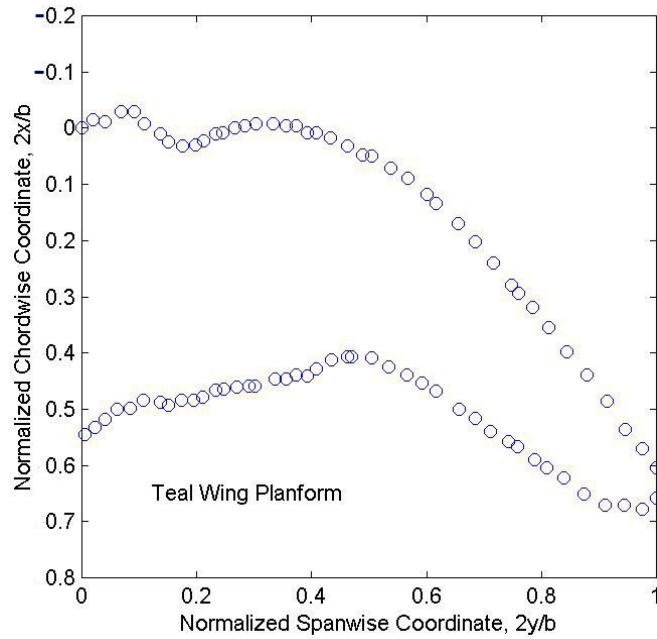


Figure 24. The planform of the Teal wing.

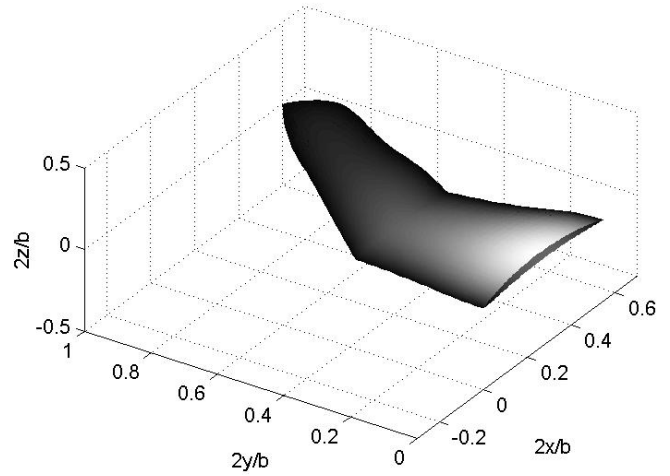


Figure 26. The generated surface of the Teal wing.

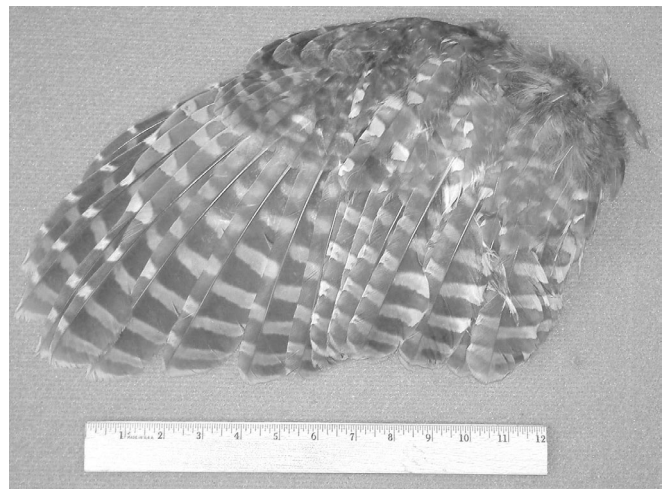


Figure 27. The Owl wing.

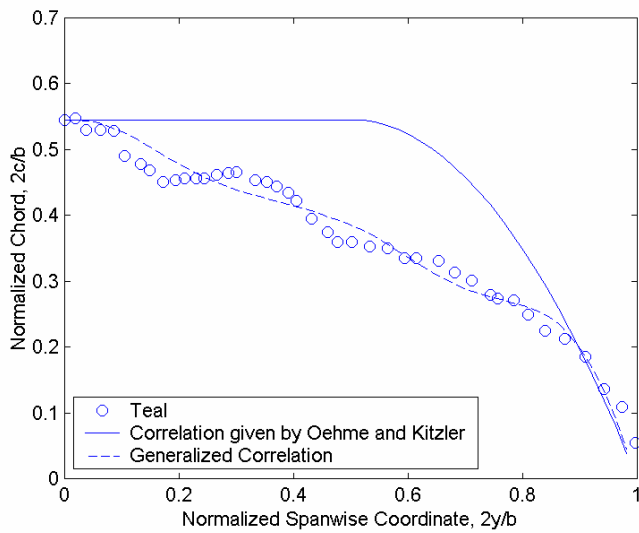


Figure 25. The chord distribution of the Teal wing.

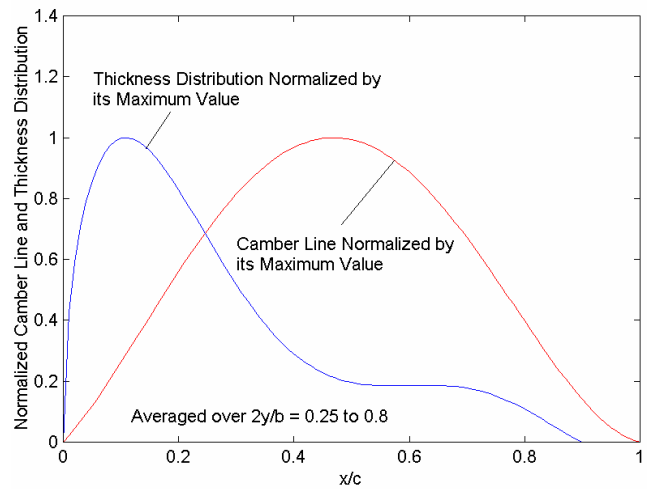


Figure 28. The camber line and thickness distribution of the Owl wing.

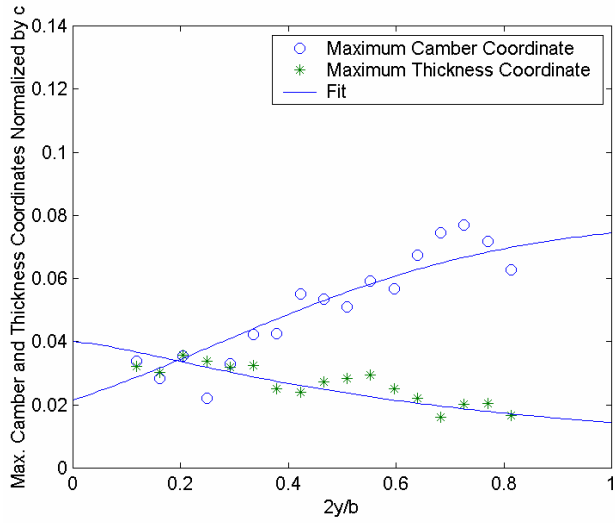


Figure 29. The maximum camber and thickness coordinates as a function of the spanwise location for the Owl wing.

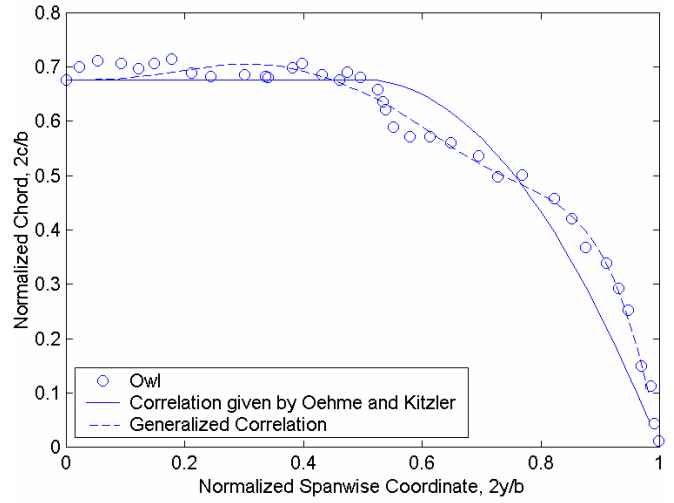


Figure 31. The chord distribution of the Owl wing.

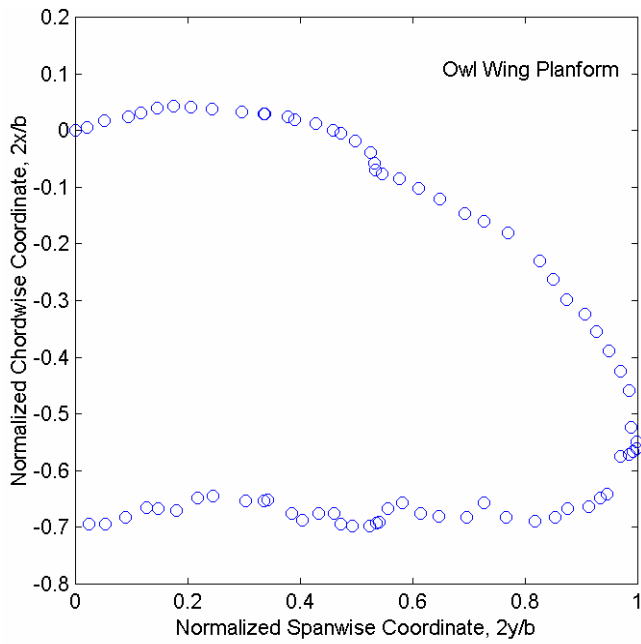


Figure 30. The planform of the Owl wing.

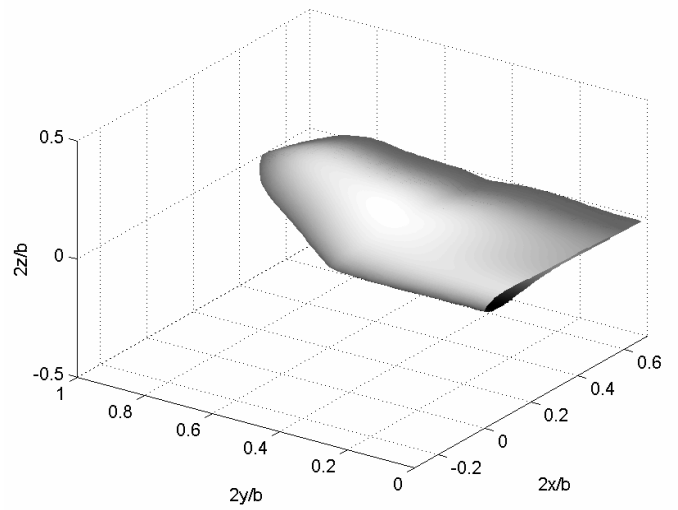


Figure 32. The generated surface of the Owl wing.

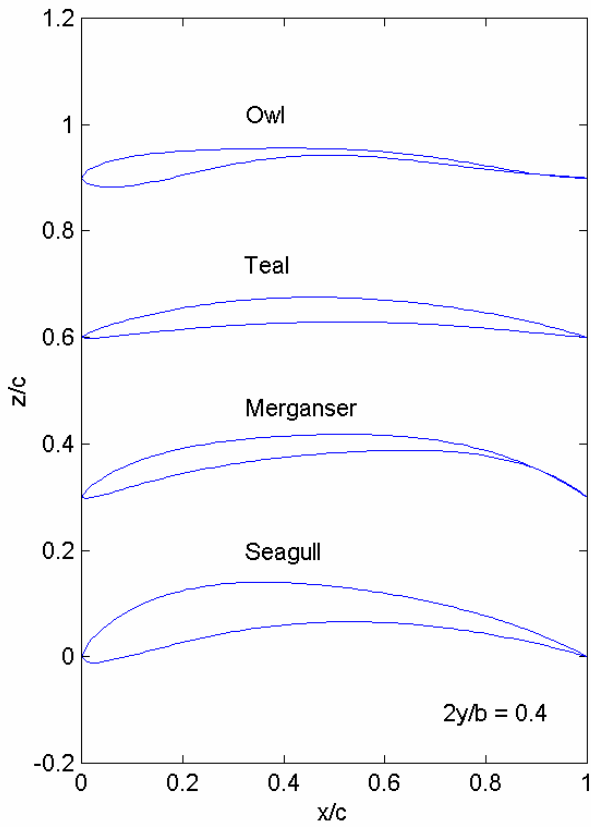


Figure 33. Airfoil sections of the avian wings at $2y/b = 0.4$.

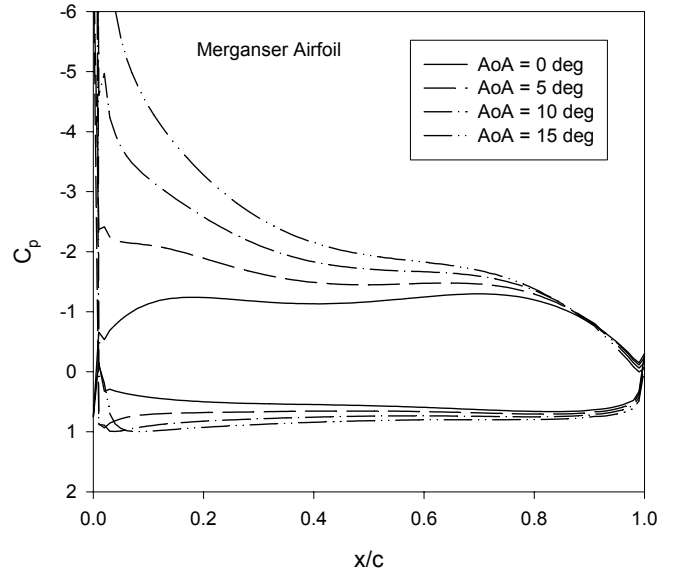


Figure 35. The pressure coefficient distributions of the Merganser wing at different angles of attack.

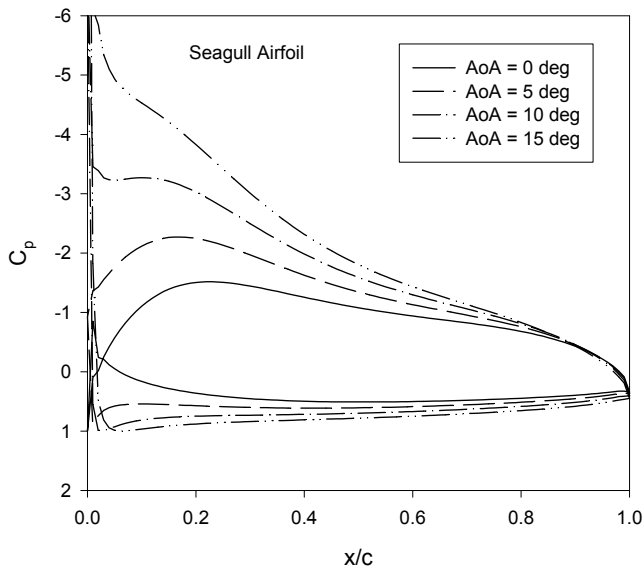


Figure 34. The pressure coefficient distributions of the Seagull wing at different angles of attack.

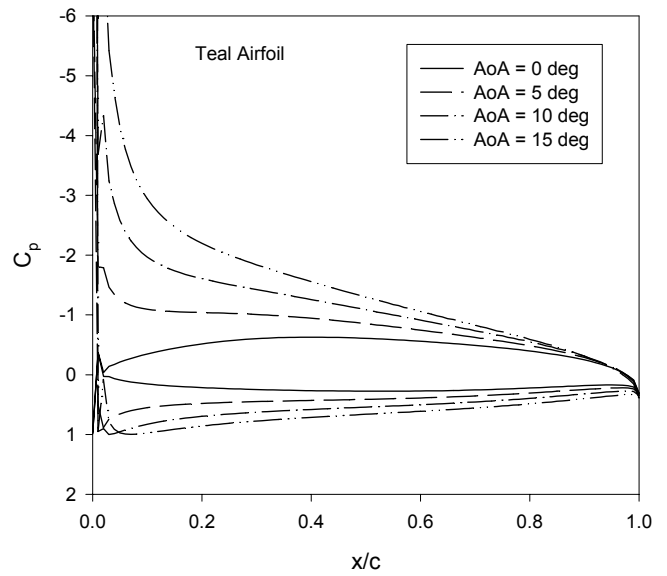


Figure 36. The pressure coefficient distributions of the Teal wing at different angles of attack.

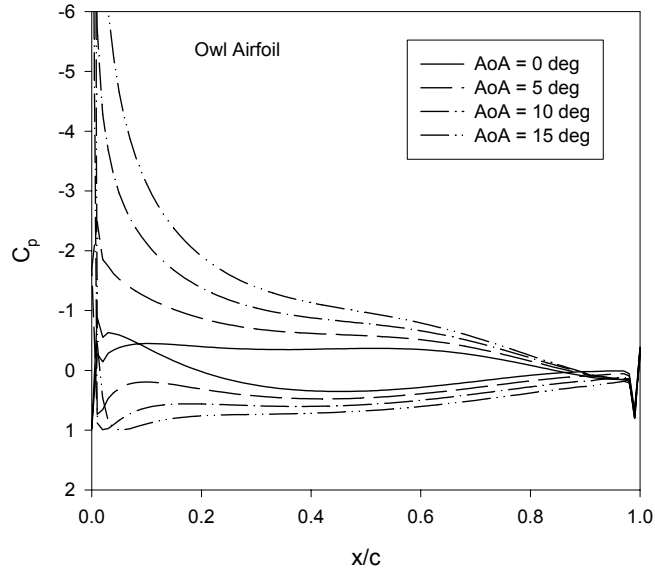


Figure 37. The pressure coefficient distributions of the Owl wing at different angles of attack.

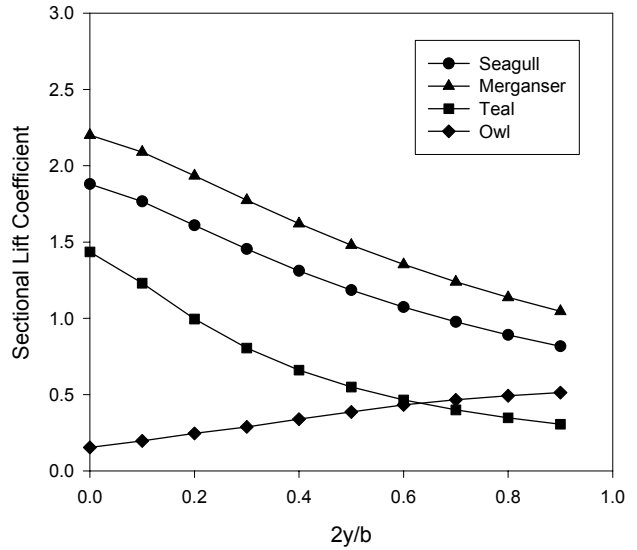


Figure 39. The sectional lift coefficient distributions along the wing span for the Seagull, Merganser, Teal and Owl wings at AoA = 0 degree.

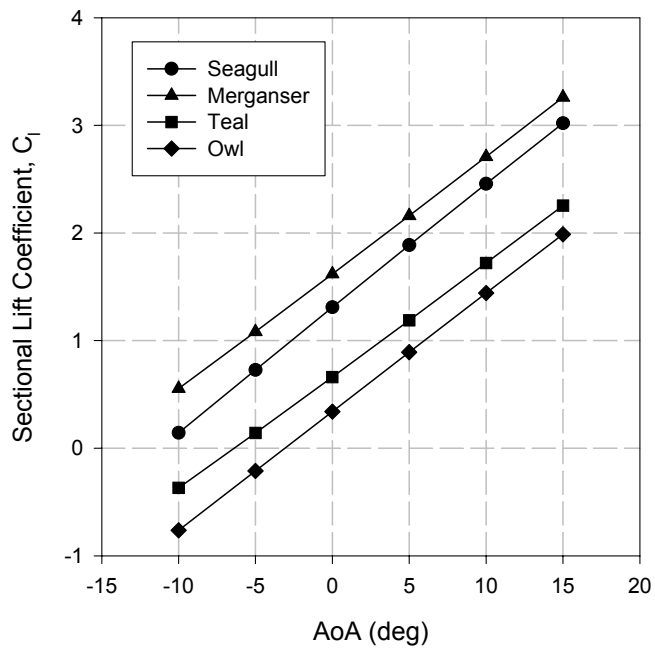


Figure 38. The sectional lift coefficient as a function of the angles of attack.

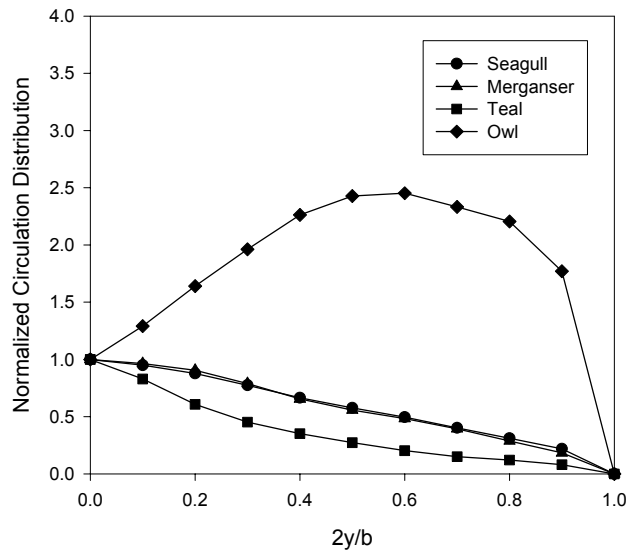


Figure 40. The normalized circulation distributions along the wing span for the Seagull, Merganser, Teal and Owl wings.

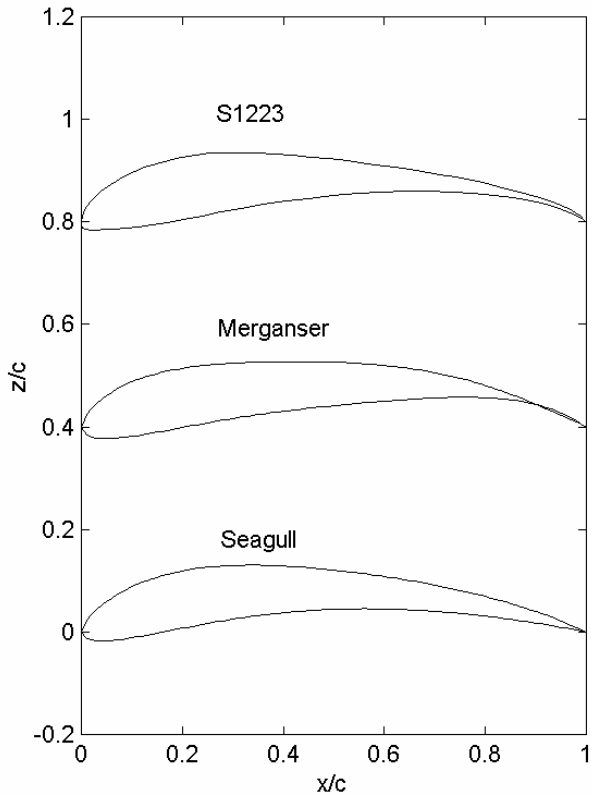


Figure 41. The high-lift low Reynolds airfoil S1223 compared to the Seagull and Merganser airfoils with the same maximum camber line and thickness coordinates.

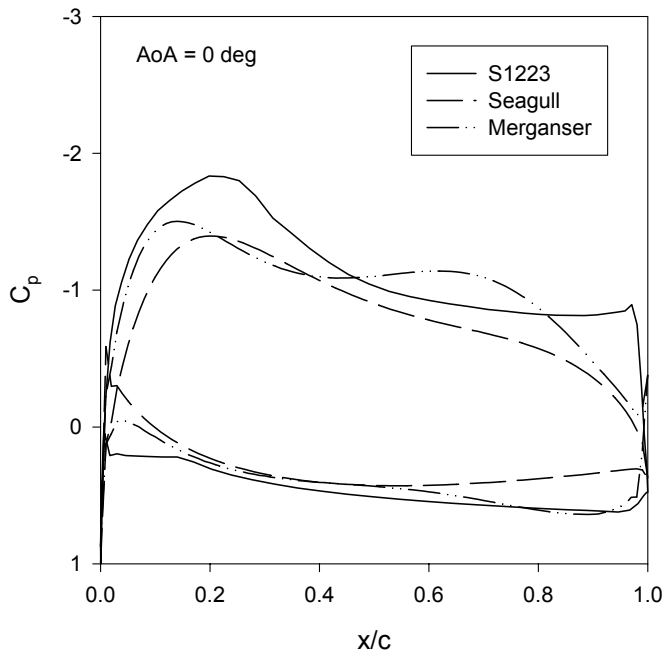


Figure 42. The pressure coefficient distributions for the Seagull and Merganser airfoils along with that for S1223 at AoA = 0 degree.

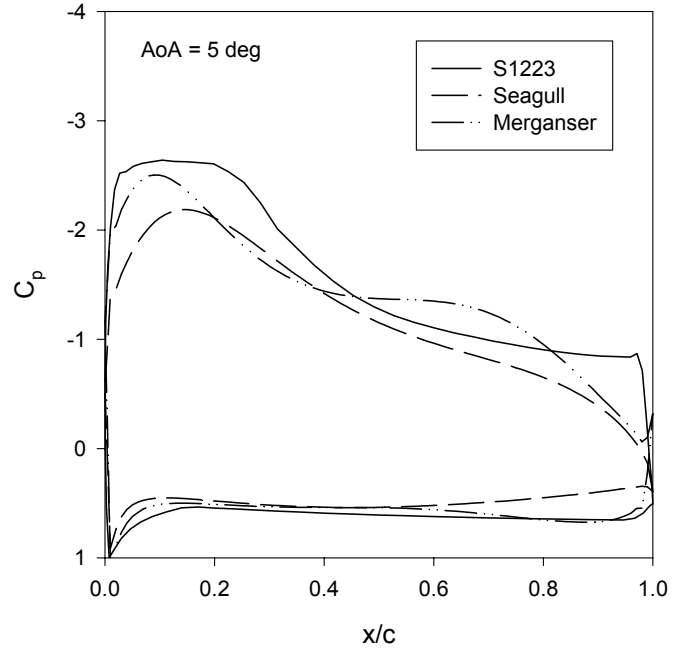


Figure 43. The pressure coefficient distributions for the Seagull and Merganser airfoils along with that for S1223 at AoA = 5 degrees.

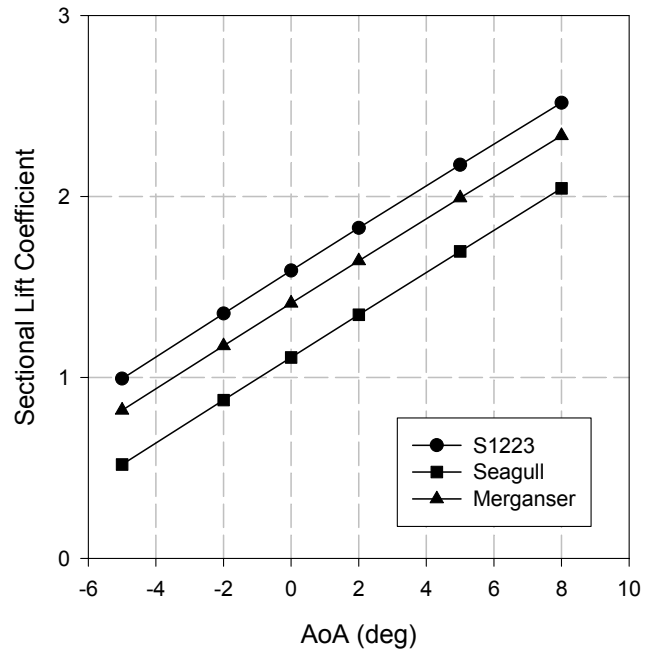


Figure 44. The sectional lift coefficient as a function of AoA for the S1223, Seagull and Merganser airfoils.

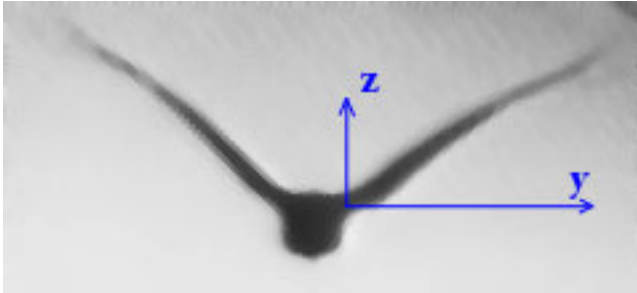


Figure 45. An image of a level-flying crane viewed by a camera directly from the front.

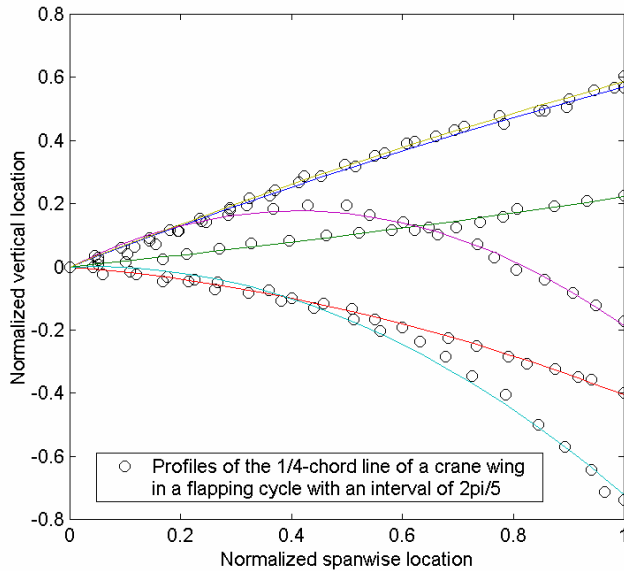


Figure 46. The profiles of the front-projected 1/4-chord line of the flapping crane wing at different instants.

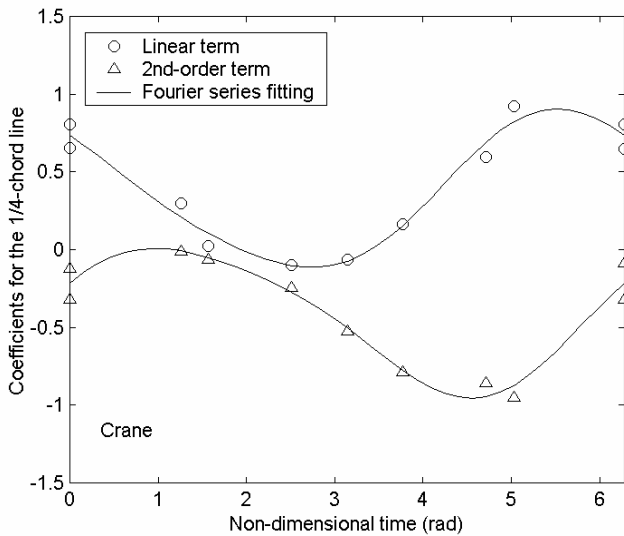


Figure 47. The polynomial coefficients of the front-projected 1/4-chord line of the flapping crane wing as a function of time.

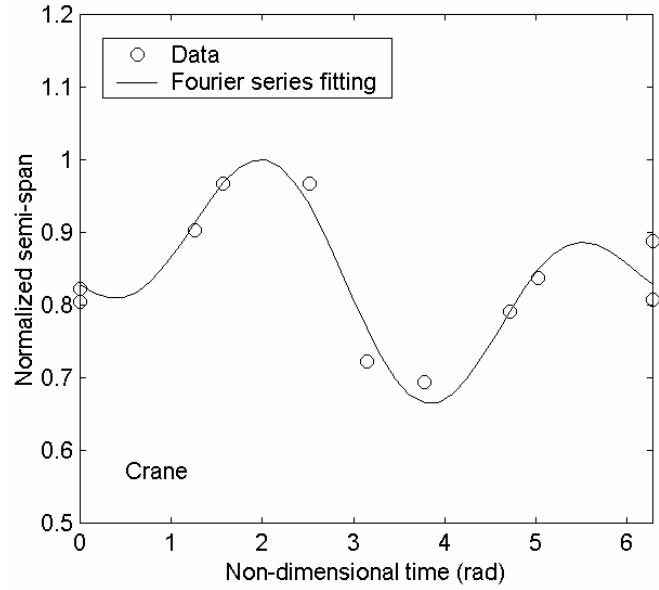


Figure 48. The orthographically projected semi-span $b/2$ normalized by $\max(b/2)$ for the flapping crane wing as a function of time.

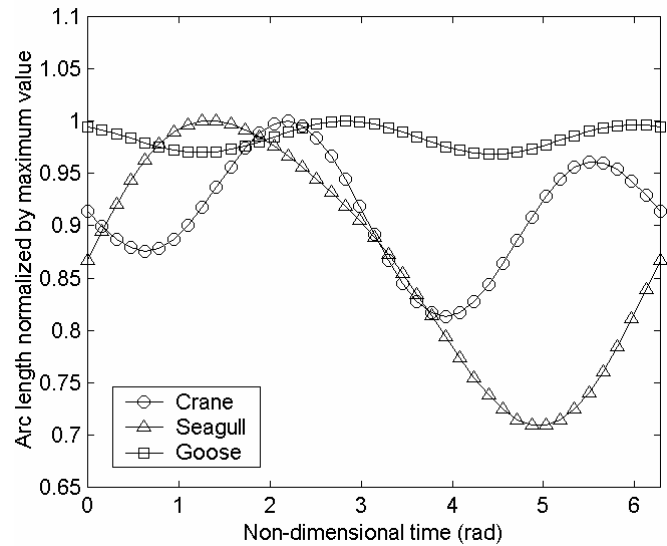


Figure 49. The normalized arc length of the front-projected 1/4-chord line of the flapping crane, seagull and goose wings as a function of time.

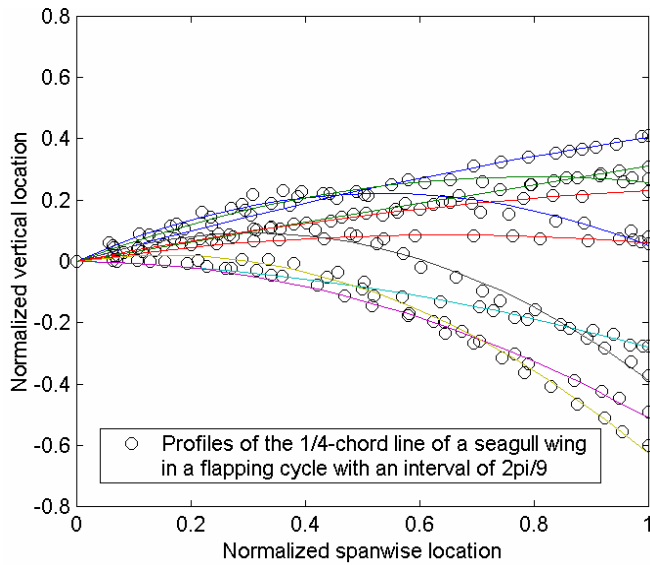


Figure 50. The profiles of the front-projected 1/4-chord line of the flapping seagull wing at different instants.

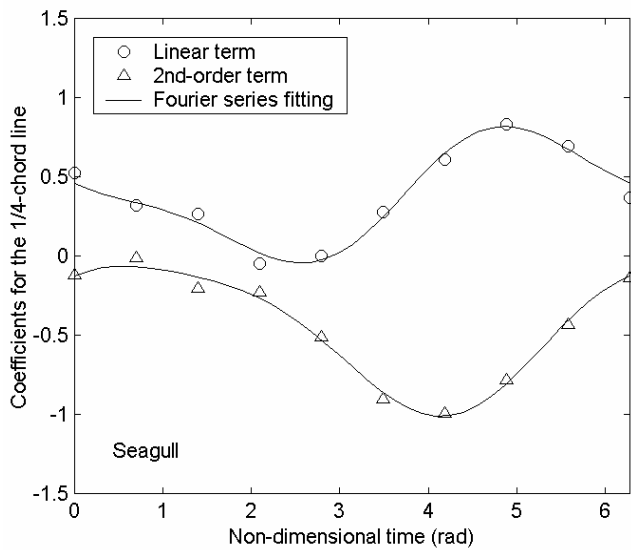


Figure 51. The polynomial coefficients of the front-projected 1/4-chord line of the flapping seagull wing as a function of time.

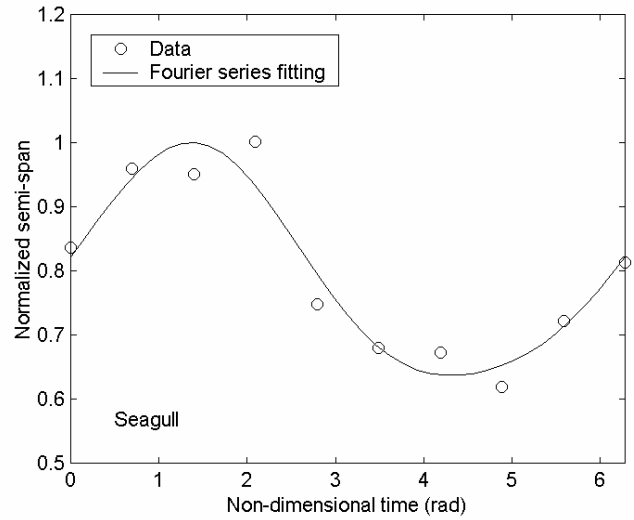


Figure 52. The orthographically projected semi-span $b/2$ normalized by $\max(b/2)$ for the flapping seagull wing as a function of time.

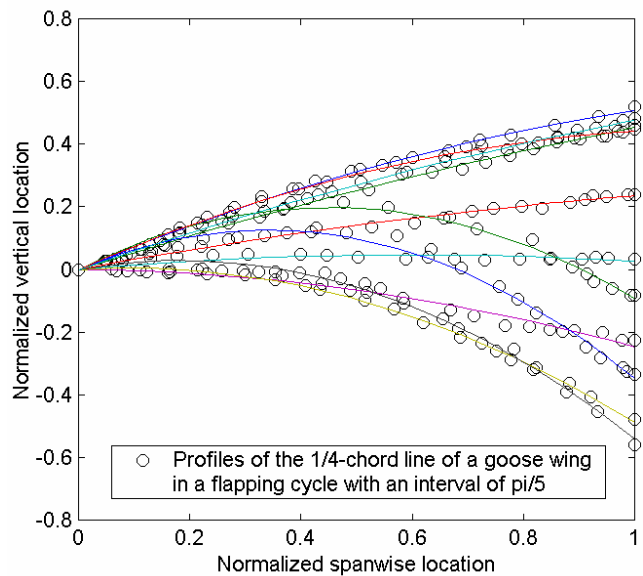


Figure 53. The profiles of the front-projected 1/4-chord line of the flapping goose wing at different instants.

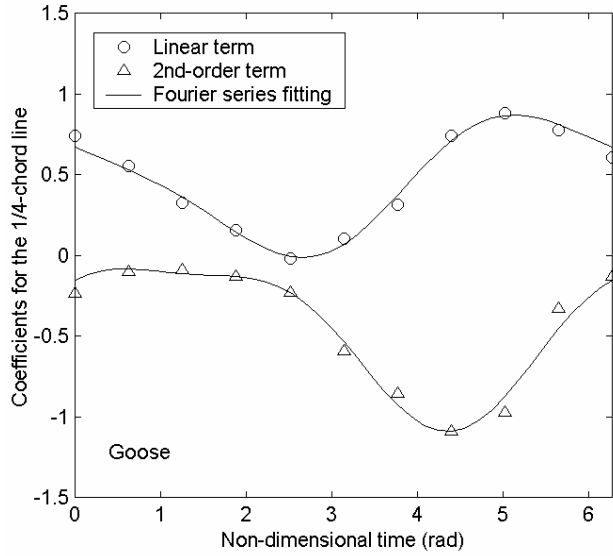


Figure 54. The polynomial coefficients of the front-projected 1/4-chord line of the flapping goose wing as a function of time.

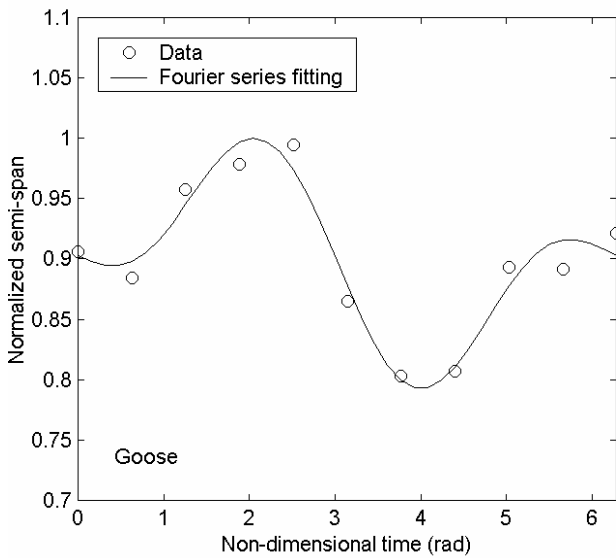


Figure 55. The orthographically projected semi-span $b/2$ normalized by $\max(b/2)$ for the flapping goose wing as a function of time.

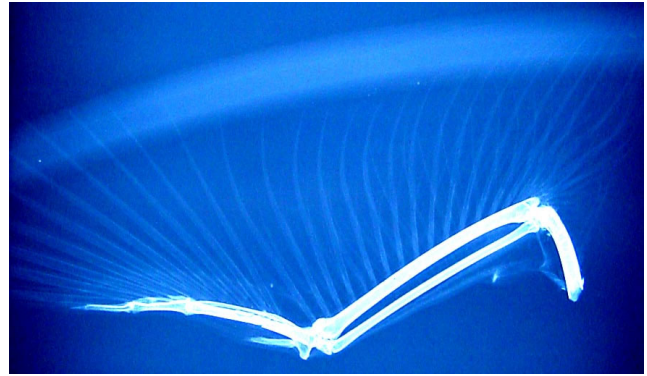


Figure 56. An X-ray image of a seagull wing.

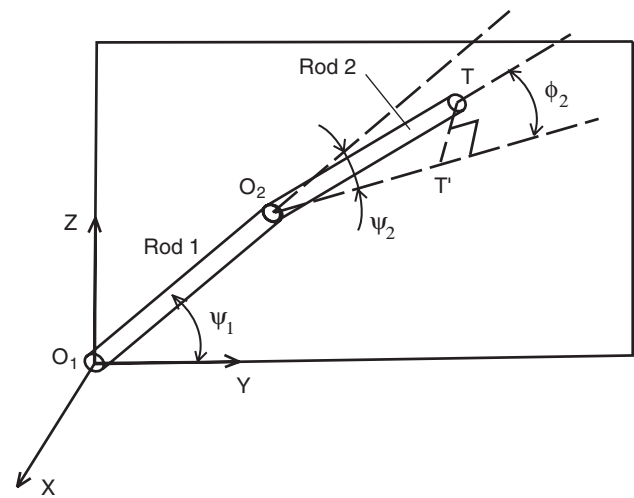


Figure 57. Two-jointed arm system.

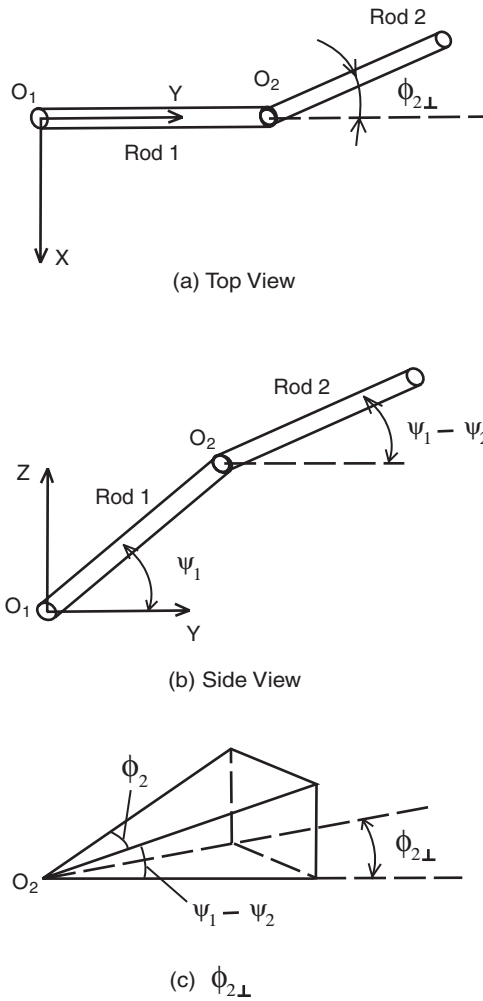


Figure 58. Projected views of a two-jointed arm system. (a) top view, (b) side view, (c) the meaning of the angle $\phi_{2\perp}$.

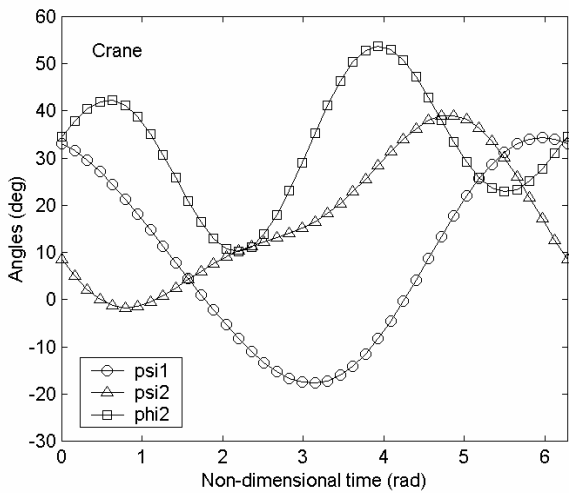


Figure 59. The angles ψ_1 , ψ_2 and ϕ_2 as a function of time for the crane wing.

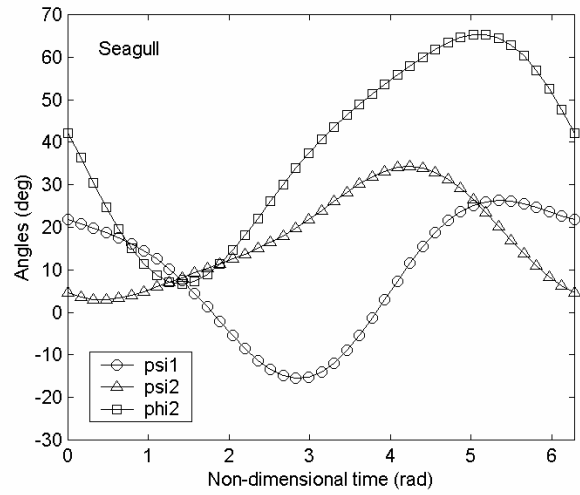


Figure 60. The angles ψ_1 , ψ_2 and ϕ_2 as a function of time for the seagull wing.

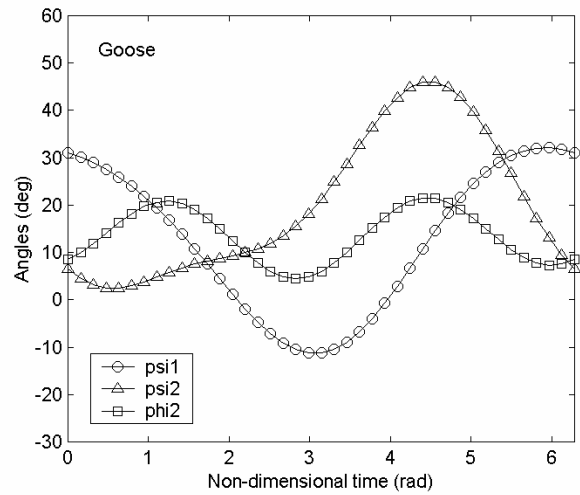


Figure 61. The angles ψ_1 , ψ_2 and ϕ_2 as a function of time for the goose wing.

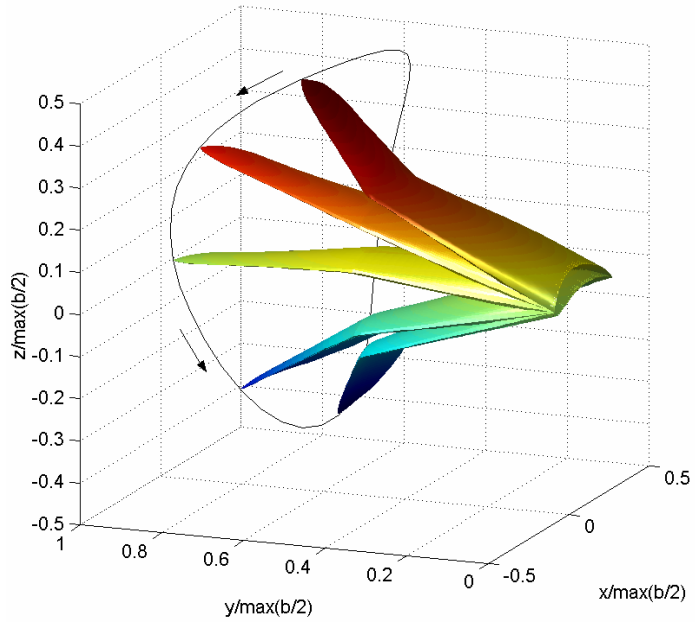


Figure 62. Re-constructed flapping seagull wing at $\omega t = 0, \pi/4, \pi/2, 3\pi/4$ and π .